PHYSICAL REVIEW X **15,** 011009 (2025)

# Spectroscopy and Modeling of $^{171}$Yb Rydberg States for High-Fidelity Two-Qubit Gates

Michael Peper,[1] Yiyi Li,[1] Daniel Y. Knapp,[1,2,*] Mila Bileska,[1,2] Shuo Ma,[1,2] Genyue Liu,[1] Pai Peng,[1]
Bichen Zhang,[1] Sebastian P. Horvath,[1] Alex P. Burgers,[1,†] and Jeff D. Thompson[1,‡]
[1]*Department of Electrical and Computer Engineering, Princeton University,*
*Princeton, New Jersey 08544, USA*
[2]*Department of Physics, Princeton University, Princeton, New Jersey 08544, USA*

(Received 8 June 2024; accepted 6 December 2024; published 17 January 2025)

Highly excited Rydberg states and their interactions play an important role in quantum computing and simulation. These properties can be predicted accurately for alkali atoms with simple Rydberg level structures. However, an extension of these methods to more complex atoms such as alkaline-earth atoms has not been demonstrated or experimentally validated. Here, we present multichannel quantum defect models for highly excited $^{174}$Yb and $^{171}$Yb Rydberg states with $L \leq 2$. The models are developed using a combination of existing literature data and new, high-precision laser and microwave spectroscopy in an atomic beam, and validated by detailed comparison with experimentally measured Stark shifts and magnetic moments. We then use these models to compute interaction potentials between two Yb atoms, and find excellent agreement with direct measurements in an optical tweezer array. From the computed interaction potential, we identify an anomalous Förster resonance that likely degraded the fidelity of previous entangling gates in $^{171}$Yb using $F = 3/2$ Rydberg states. We then identify a more suitable $F = 1/2$ state, and achieve a state-of-the-art controlled-z gate fidelity of $\mathcal{F} = 0.994(1)$, with the remaining error fully explained by known sources. This work establishes a solid foundation for the continued development of quantum computing, simulation, and entanglement-enhanced metrology with Yb neutral atom arrays.

DOI: 10.1103/PhysRevX.15.011009 Subject Areas: Atomic and Molecular Physics, Quantum Physics

## I. INTRODUCTION

Rydberg-mediated interactions between neutral atoms in optical tweezer arrays are enabling for quantum computing, simulation, and quantum-enhanced metrology [1–4]. To realize high-fidelity operations, a detailed understanding of the properties of the Rydberg states and their interactions is required. Alkali atoms such as Rb or Cs can be described by simple quantum defect models, which have been validated by extensive spectroscopy [5–11]. This allows the wave functions, and in turn, matrix elements, interaction potentials, and decay rates to be computed [12–14]. Experimental studies have confirmed the predicted interaction potentials [15–17] and decay rates [18–20]. A particularly stringent test of the interaction model comes from spectroscopy of so-called macrodimer states [21–24].

Many recent experiments have focused on divalent alkaline-earth-like atoms, in particular, Sr [25–28] and Yb [29–32]. Tweezer arrays of $^{88}$Sr Rydberg atoms have been used to study many-body dynamics [33,34] and entanglement-enhanced optical clocks [35,36]. On the other hand, $^{171}$Yb is ideal for use as a qubit for quantum computing, with demonstrated long coherence times for the pure nuclear spin qubit with $I = 1/2$ [30–32], midcircuit measurement and atom reloading [37,38], and hardware-efficient error-correction strategies [39,40].

A challenge to the continued development of divalent atomic qubits, particularly those based on $^{171}$Yb, is the relative lack of spectroscopic information and models for the behavior of the Rydberg states. The Rydberg states of divalent atoms are more complex than alkali atoms because of the presence of singlet and triplet Rydberg series, interactions between series converging to other ionization thresholds (i.e., series perturbers), and hyperfine coupling (in the case of isotopes with nuclear spin $I > 0$, such as $^{87}$Sr and $^{171}$Yb). These states can be described in the framework

---

[*] Present address: Department of Physics and Astronomy, LaserLaB, Vrije Universiteit Amsterdam, de Boelelaan 1081, 1081 HV Amsterdam, The Netherlands.

[†] Present address: Department of Electrical and Computer Engineering, College of Engineering, University of Michigan, Ann Arbor, Michigan 48109, USA.

[‡] Contact author: jdthompson@princeton.edu

of multichannel quantum defect theory (MQDT) [41,42], which in turn allows the computation of matrix elements, interaction potentials, and decay rates [43,44].

Single-channel approximations have been used to predict interaction potentials in both $^{174}$Yb and $^{88}$Sr, which both have no nuclear spin ($I = 0$) [43,45]. Moreover, relatively complete MQDT descriptions of $^{88}$Sr have been developed and used to study lifetimes and branching ratios [43], and MQDT models have been developed to fit spectroscopic data for certain Rydberg series in $^{174}$Yb [46–50]. The energies of certain Rydberg series in $^{87}$Sr ($I = 9/2$) have also been determined [51] and used to predict $C_6$ coefficients using an MDQT formalism [52]. However, to the best of our knowledge, there is no comprehensive spectroscopy or MQDT model of the Rydberg states of $^{171}$Yb, and no MQDT interaction models for divalent atoms have been experimentally verified at a level approaching the precision of alkali atom models.

In this article, we present four main results. First, we present refined MQDT models for the Rydberg states of $^{174}$Yb with $L \leq 2$ (Sec. II). This set of states is sufficient to accurately predict the interactions and polarizability of the $L = 0$ states that are most frequently used in experiments. This extends prior work [46,49,50,53–61] by incorporating new spectroscopic measurements and refitting all of the MQDT models simultaneously with a global fit for improved consistency and accuracy. Furthermore, we determine singlet-triplet mixing angles by comparison to experimental measurements of the static dipole polarizability, which are undetermined by the state energies alone [62]. We find excellent agreement with measured Rydberg state energies, polarizabilities, and magnetic moments.

Next, we extend these models to describe $^{171}$Yb states with $L \leq 2$ by including the hyperfine interaction (Sec. III). The models are refined and validated by comparison to extensive laser and microwave spectroscopy of $^{171}$Yb Rydberg states from an atomic beam apparatus. We also test the MQDT model matrix elements by comparison to measured static dipole polarizabilities and magnetic moments, finding excellent agreement.

Third, we use the $^{171}$Yb MQDT models to compute the interaction potential for Rydberg atom pairs, which we verify against direct measurements using pairs of atoms in an optical tweezer array (Sec. IV). We show that the $^{171}$Yb $F = 3/2$ Rydberg state that was previously used to implement entangling gates [31,40] has a surprisingly small Förster defect (< 10 MHz) over a large range of effective principal quantum number $\nu$. The small Förster defect gives rise to an imperfect blockade, and we conjecture that it is responsible for the discrepancy between the measured [$\mathcal{F} = 0.980(1)$] and predicted ($\mathcal{F}_{\mathrm{th}} = 0.989$) gate error in Ref. [40].

Finally, in Sec. V we leverage these models to predict that certain $F = 1/2$ states should have a larger Förster defect, giving rise to a cleaner blockade and improved gate fidelity. We then experimentally demonstrate improved gates with $\mathcal{F} = 0.994(1)$. Importantly, the dominant remaining errors are well understood (arising from Rydberg state decay and Doppler shifts), which is promising for future improvements in gate fidelity with increased laser power.

This work solidifies the foundation for future quantum computing, simulation, and quantum-enhanced metrology applications of $^{171}$Yb Rydberg atoms. The developed MQDT models not only reproduce the energies of ytterbium Rydberg states, but also enable an accurate prediction of matrix elements, polarizabilities, and Rydberg interactions within a self-consistent framework. This comprehensive approach also establishes the basis for treating other complex atomic systems including $^{87}$Sr [63] and lanthanide atoms such as Ho [64] or Er [65].

## II. MULTICHANNEL QUANTUM DEFECT MODEL OF $^{174}$Yb

Figure 1(a) illustrates the basic principle of MQDT, in the context of $^{174}$Yb (the most abundant isotope, with nuclear spin $I = 0$). The ground state of $^{174}$Yb has the electronic configuration $[\mathrm{Xe}]4f^{14}6s^2$, and the states of primary interest are singly excited states $[\mathrm{Xe}]4f^{14}6sn\ell$, where $n$, $\ell$ are the principal quantum number and orbital angular momentum of the excited electron (the Xe core and $4f^{14}$ electrons are omitted henceforth, unless otherwise noted). These states are approximately described in $LS$ coupling by the term symbol $^{2S+1}L_J$ with total electron spin $S = \{0, 1\}$, $L = \ell$, and total electronic angular momentum $J$. In single-channel quantum defect theory, these states form isolated series converging to the ground state of the $^{174}$Yb$^+$ ion with the electron configuration $6s^1$. The energy of the states in this series is $E_n = I_{6s} - R/\nu_{6s}^2$, where $\nu_{6s} = n - \mu$ is the effective quantum number, and $\mu(n, L, J)$ is the quantum defect that captures the interaction with the core for that series, with only weak dependence on $n$.

Compared to lighter divalent atoms such as Sr, this picture is complicated for Yb by a relatively high density of low-lying excited states in Yb$^+$, which give rise to doubly excited states in the energy range of interest (e.g., $[\mathrm{Xe}]4f^{14}6pn\ell$). These doubly excited states are part of additional Rydberg series converging to higher thresholds [Fig. 1(a)] and couple to the singly excited Rydberg states of interest through configuration interactions, which mix series with the same $J$ and parity. This interaction alters the energy spectrum through level repulsion (i.e., series perturbers), which gives rise to sharp variations in $\mu$ with $n$, and correspondingly modifies the wave functions needed to compute quantities of interest such as matrix elements, interactions, and lifetimes. This effect can be described quantitatively using MQDT, treating the interacting series as a set of coupled channels and parametrizing the

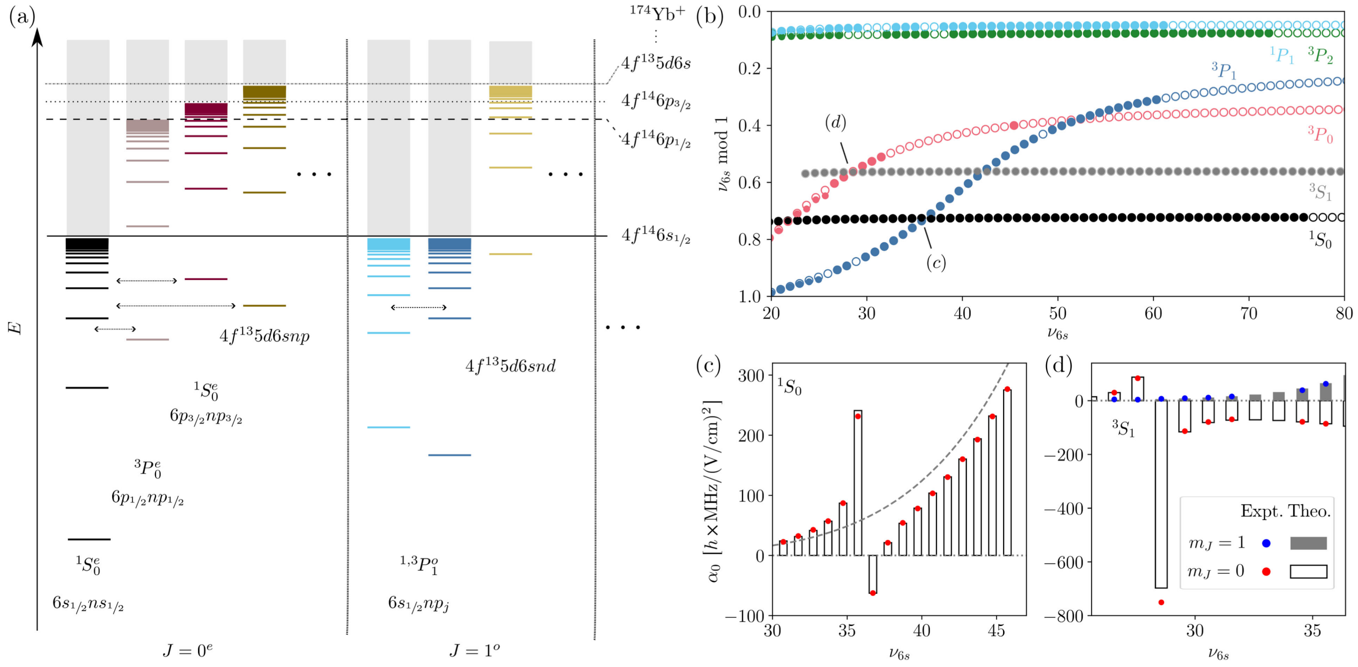

FIG. 1. (a) Schematic diagram of several Rydberg series $^{174}$Yb illustrating the principle of MQDT. Both singly excited ($6s_{1/2}n\ell$) and doubly excited (e.g., $6pn\ell$) series are included, converging to different thresholds corresponding to excited states of the $^{174}$Yb$^+$ ion (note that in this schematic diagram, the energy-level spacings are not to scale, and only the subset of channels most relevant for the presented MQDT models are included). The Rydberg series are sorted by total angular momentum $J$ and parity (even and odd denoted by $e$ and $o$ superscripts, respectively). $LS$ coupling term symbols are written where possible (i.e., $^1S_0$). Configuration interactions mix series with the same $J$ and parity, as indicated by the horizontal arrows. (b) Lu-Fano-like plot of the $L = 0$ and $L = 1$ Rydberg series of $^{174}$Yb, showing the fractional part of the quantum defect ($\nu_{6s}$ mod 1) as a function of the effective principal quantum number $\nu_{6s}$. The open circles show the eigenstates predicted by the MQDT model, while the filled circles show experimentally determined energies. (c) Static dipole polarizability $\alpha_0$ [see Eq. (B1)] of the $n$ $^1S_0$ series close to a level crossing with the $n$ $^3P_1$ series (red points, experiment; bars, MQDT prediction). The gray dashed line indicates the expected $\nu^7$ scaling in the absence of singlet-triplet mixing. (d) Static dipole polarizability $\alpha_0$ of the $n$ $^3S_1$ series near a crossing with $n$ $^3P_0$. The experimental data for the polarizability of the $m_J = 0$ (red) and $m_J = 1$ (blue) states agree well with the theoretical predictions from the MQDT model. The error bars on the experimental data points in panels (c) and (d) represent the standard error from fitting the observed Stark shifts to Eq. (B1).

interactions with a small number of mixing angles or a $K$ matrix [66,67]. We give a pedagogical introduction of the MQDT approach in Appendix A.

Previous work in $^{174}$Yb has reported spectroscopic measurements of certain $S$, $P$, $D$, and $F$ states, along with MQDT models that adequately reproduce their energy spectrum [29,46–49] (a comprehensive summary can be found in Ref. [50]). We improved these models by performing additional microwave spectroscopy of some $P$ Rydberg states between $n = 30$ and 50 (using an atomic beam apparatus; Appendix B). The resulting MQDT model is summarized in Fig. 1(b).

However, mixing between channels converging to the same threshold (i.e., singlet-triplet mixing) does not alter the state energies [62] but can significantly alter wave functions and matrix elements [68]. To develop an MQDT model with accurate wave functions, we augment the traditional approach of fitting the energy levels with additional measurements of the static dipole polarizability of the atomic states, which depend directly on the matrix elements and wave functions.

In Fig. 1(c), we present measurements of the static dipole polarizability (red dots) for the $^1S_0$ series near its crossing with $^3P_1$. By adjusting the single-triplet mixing angle in the $^{1,3}P_1$ MQDT model, we can accurately capture the resonancelike feature, which deviates strongly from the usual $\nu^7$ polarizability trend [69]. The final model predicts a triplet character of the $^1P_1$ Rydberg series that varies between 6.30 (3)% for $n = 40$ and 2.96(16)% for $n = 100$, which is consistent with previous estimates based on measurements of diamagnetic shifts [57] but considerably more precise (Appendix D 2). As an additional check of the predicted MQDT wave functions, we characterize the scalar and tensor polarizability of the $n$ $^3S_1$ Rydberg series near its crossing with $^3P_0$, finding excellent agreement [Fig. 1(d)]. The measured polarizabilities of the $6sns$ $^1S_0$ and $6sns$ $^3S_1$ states are summarized in Supplemental Material [70].

Through a similar analysis of the $^{1,3}D_2$ using literature data for the magnetic moments of these states [59], we find a triplet character of $n$ $^1D_2$ Rydberg states of approximately 15% (details in Appendix D 5).

Other details of the spectroscopy are presented in Appendix B. A complete tabulation of the model parameters and the compiled spectroscopic data are presented in Supplemental Material [70]. A more detailed description of the developed MQDT models is presented in Appendix D.

## III. MQDT MODEL OF $^{171}$Yb

In contrast to $^{174}$Yb, $^{171}$Yb has a nonzero nuclear spin of $I = 1/2$. The absence of hyperfine coupling in low-lying $J = 0$ manifolds (i.e., $^1S_0$ or $^3P_0$) results in an ideal nuclear spin qubit [30,31,63]. Counterintuitively, the Rydberg states of $^{171}$Yb have a fairly strong hyperfine coupling, which arises from the interplay of hyperfine coupling in the Yb$^+$ core and the exchange interaction between the core and Rydberg electrons. This coupling is necessary to implement entangling gate operations on the pure nuclear spin qubit [31,40], but also significantly complicates the description of the Rydberg series [51,75–77]. We note that the role of hyperfine coupling in $^{171}$Yb qubits is almost opposite to alkali atoms, where the ground state has strong hyperfine coupling, while direct hyperfine coupling of the Rydberg state can be largely neglected [78].

In the context of MQDT, hyperfine effects can be represented as a coupling between multiple Rydberg series with the same parity and total angular momentum $F$ converging to different thresholds corresponding to the hyperfine-split ion-core states (Fig. 2). In the case of $^{171}$Yb$^+$, the $6s\,^2S_{1/2}$ ground state is split into two hyperfine states with total angular momentum $F_c = 0$ and $F_c = 1$, separated by $A_{\mathrm{HF}} = 12.642\,812$ GHz [79]. For the range of $\nu$ relevant for quantum information applications ($40 \lesssim \nu \lesssim 100$), the hyperfine interaction energy is comparable to the spacing between principal quantum levels, resulting in strong channel mixing when there is more than one series with the same $F$ and parity [80]. For example, the $6sns$ states in $^{171}$Yb give rise to two coupled $F = 1/2$ series converging to $F_c = 0$ and $F_c = 1$, and a single $F = 3/2$ series converging to the $F_c = 1$ threshold.

The effect of hyperfine-induced channel mixing has been experimentally studied previously in several species, including $^{87}$Sr [51,76,81,82] and $^{135,137}$Ba [47,83]. However, only a small number of measurements of $^{171}$Yb Rydberg states have been reported [31,71,84,85].

### A. $L = 0$ states

There are three Rydberg series with $L = 0$ in $^{171}$Yb (Fig. 2). At low $\nu$, where hyperfine coupling is a small perturbation compared to the singlet-triplet splitting, these series are described in the $LS$ basis as a single $^1S_0$ series with $F = 1/2$, and two $^3S_1$ series with $F = \{1/2, 3/2\}$. Very close to the threshold, $jj$ coupling is more appropriate: One $F = 1/2$ series results from adding the outer electron spin ($s = 1/2$) to the $F_c = 0$ ion core, while the other $F = 1/2$ and $F = 3/2$ series are connected to $F_c = 1$. While these descriptions are equivalent for the $F = 3/2$ series, the $F = 1/2$ eigenstates cannot be simply described in either basis in between these limits, necessitating an MQDT model for these states.

We have experimentally measured the energy of most $L = 0$, $F = 1/2$ states with $25 < \nu < 120$ using laser spectroscopy as described in Appendix B. The measured $L = 0$ Rydberg state energies and associated MQDT model predictions are shown in Fig. 3(a). The agreement is excellent: The $F = 1/2$ states have a root-mean-squared

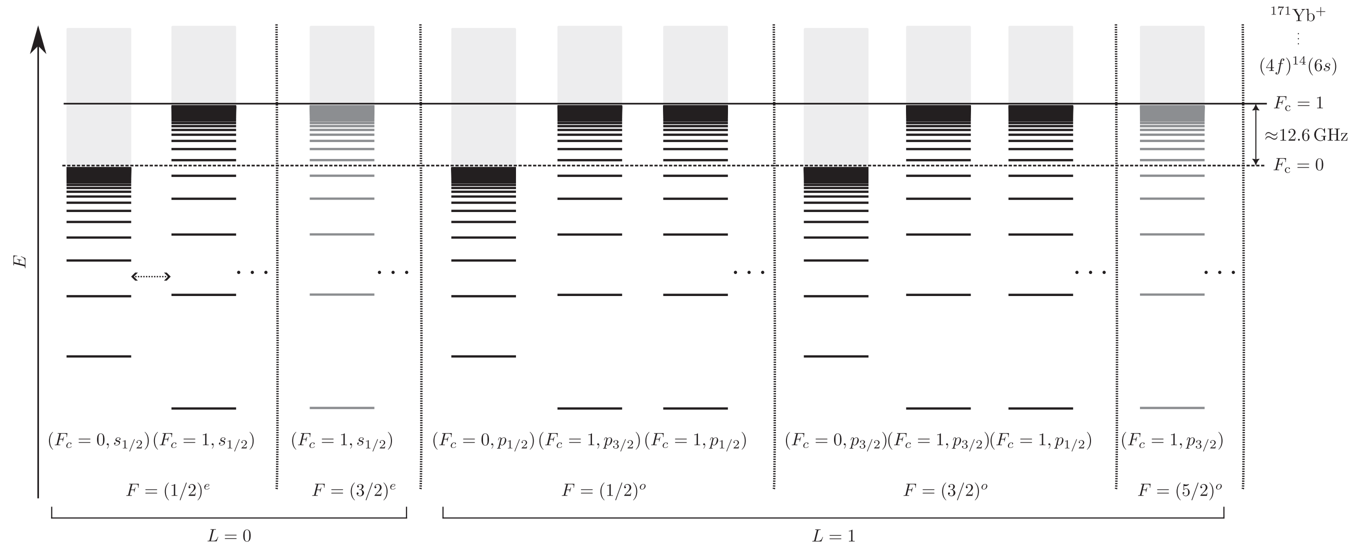

FIG. 2. Schematic energy-level diagram of the $L = 0$ and $L = 1$ Rydberg states of $^{171}$Yb, indicating Rydberg series converging to the two hyperfine states of the $^{171}$Yb$^+$ ground state. Channels converging to electronically excited states of the ion core are not shown, but are included in the MQDT models. The series are labeled by their good quantum numbers $F$ and parity (denoted by superscript $e$, for even, and $o$ for odd).

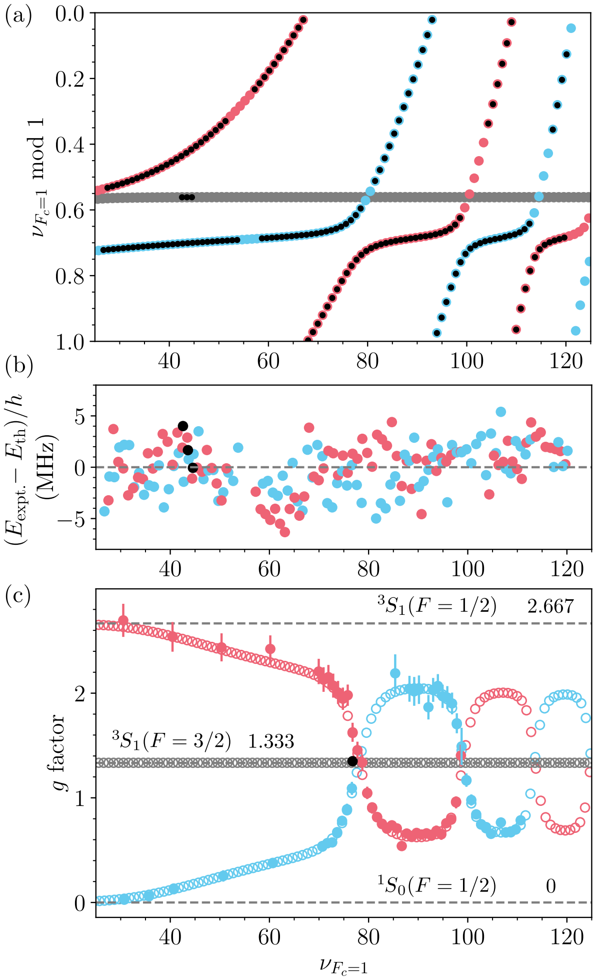

FIG. 3. (a) Lu-Fano-type plot of $^{171}$Yb $|\nu, L = 0, F = 1/2\rangle$ Rydberg states (red, blue) and $|\nu, L = 0, F = 3/2\rangle$ states (gray). The black points correspond to experimentally observed states, whereas the colored points denote bound states in the MDQT model. For $\nu < 70$, we refer to the red states as triplet connected and the blue states as singlet connected based on their dominant character in $LS$ coupling. This description breaks down at higher principal quantum numbers. (b) Deviation between measured and modeled bound-state energies (red and blue for $F = 1/2$ and black for $F = 3/2$). (c) Measured [filled circles, color code as in (b)] and predicted (empty circles) $g$ factors. The gray dashed lines indicate the Landé $g$ factors in pure $LS$ coupling. The error bars on the experimental data points represent the standard error from fitting the observed Zeeman shifts to Eq. (B2).

deviation of 2.3 MHz from the model, consistent with the $3\sigma$ uncertainty of 10 MHz of the wavelength meter used to determine the laser frequencies.

In analogy to the Stark shift measurements for $^{174}$Yb in Figs. 1(c) and 1(d), we test the wave functions by comparing the measured and predicted magnetic moments of a subset of states shown in Fig. 3(c). For low $\nu$, the magnetic moments are close to the Landé $g$ factors for $LS$-coupled states, but they deviate significantly above $\nu = 40$.

The primary characteristic of the $F = 1/2$ series is the avoided crossings in the energy spectrum. These can be understood from the channel structure of Fig. 2: Strong channel mixing and level repulsion occur when the separation between Rydberg levels is comparable to the ion-core hyperfine splitting. For $^{171}$Yb, the $\Delta n = 1$, 2, and 3 level crossings occur at $\nu \approx 80$, 100, and 115, respectively, though we note that the wave-function character is already affected far below the first avoided crossing at $\nu = 80$. The physical mechanism for this mixing is the exchange interaction between the inner and outer electrons.

The coloring of the curves in Fig. 3 is a guide to the eye. The transition from $LS$- to $jj$-coupled states makes it challenging to introduce an unambiguous partition of all of the $F = 1/2$ states into two series. Throughout this paper, we identify specific states by $F$, $\ell$, and the effective principal quantum number $\nu$ specified to two decimal places (e.g., $|\nu = 54.28, L = 0, F = 1/2, m_F = 1/2\rangle$). In this description, $L$ is the Rydberg electron angular momentum in the $6sn\ell$ channels. In the specific case of the $F = 1/2$ S states, we also find it convenient to refer to the states with $\nu < 70$ as being "triplet connected" or "singlet connected" based on their dominant character in $LS$ coupling.

Hyperfine coupling does not affect the $F = 3/2$ series, which follows the same behavior as the $^3S_1$ series in $^{174}$Yb, converging to the $F_c = 1$ ionization limit. We have measured the energies of several $F = 3/2$ states to confirm this behavior [Fig. 3(a)].

The MQDT model parameters, tables of measured energy levels for $S$ $F = 1/2$ and $S$ $F = 3/2$, as well as Landé $g$ factors and values of dc polarizabilities of $S$ $F = 1/2$ Rydberg states are presented in Supplemental Material [70].

### B. $L = 1$ states

There are seven $L = 1$ series in $^{171}$Yb. In $LS$ coupling, they can be described as $^3P_0(F = 1/2)$, $^1P_1(F = \{1/2, 3/2\})$, $^3P_1(F = \{1/2, 3/2\})$, and $^3P_2(F = \{3/2, 5/2\})$. In $^{174}$Yb, spin-orbit coupling mixes the two $J = 1$ series as discussed in Sec. II; in $^{171}$Yb, hyperfine coupling additionally mixes the three $F = 1/2$ series and the three $F = 3/2$ series (Fig. 2).

We have experimentally measured the energies of a number of $|\nu, L = 1, F = 1/2\rangle$ and $|\nu, L = 1, F = 3/2\rangle$ states using microwave transitions from $|\nu, L = 0, F = 1/2\rangle$ states (for details, refer to Appendix B). The results are shown in Fig. 4, along with previously published measurements of low-$\nu$ states from three-photon laser spectroscopy [71,85].

As in the case of the $|\nu, L = 0, F = 1/2\rangle$ series, we begin with the $^{174}$Yb MQDT models of $^{1,3}P_1$ and $^3P_0$ (for $F = 1/2$) and $^{1,3}P_1$ and $^3P_2$ (for $F = 3/2$) presented in Appendix D and refine the model by a global fit to the

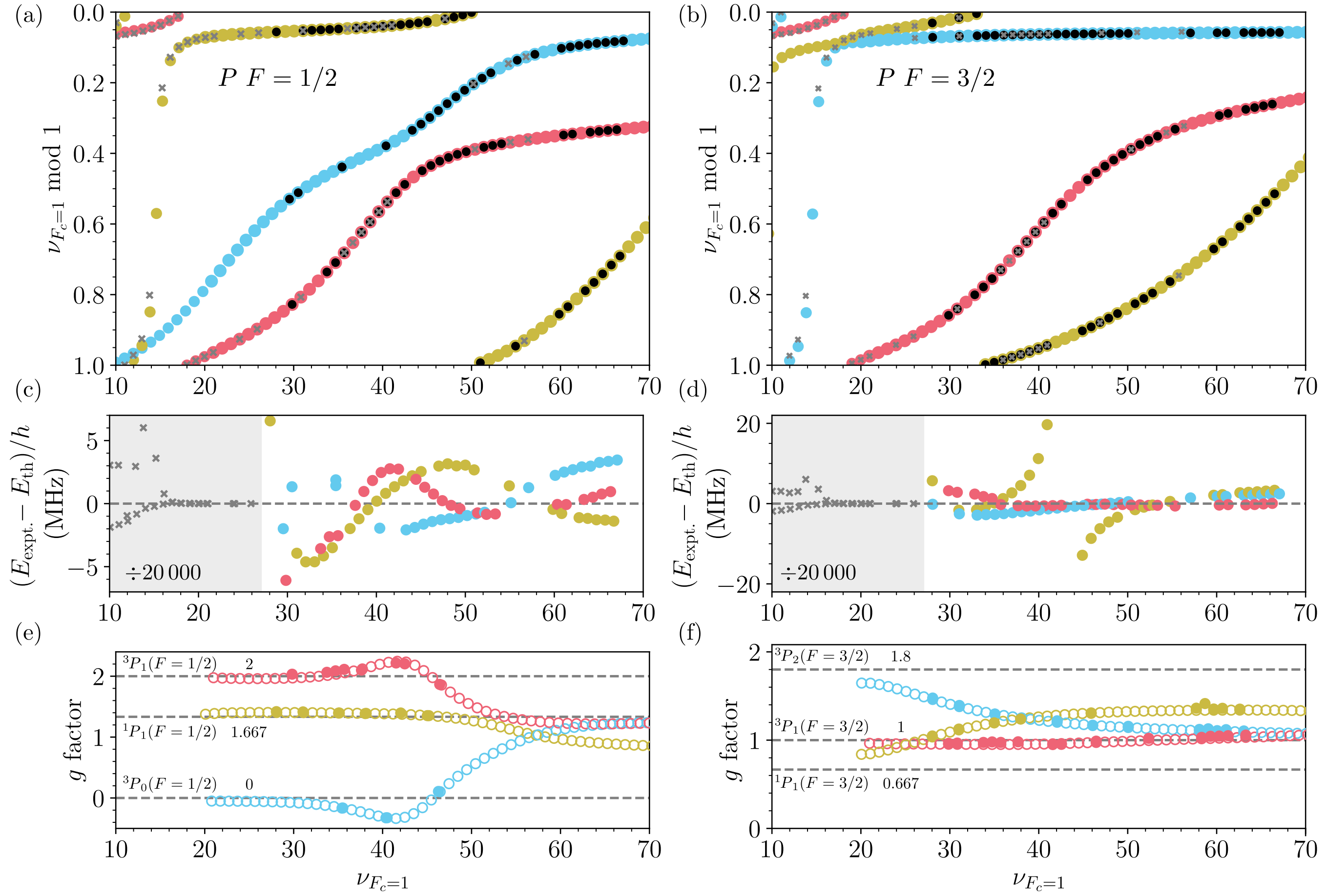

FIG. 4. (a),(b) Lu-Fano-type plot of $^{171}$Yb $|\nu, L = 1, F = 1/2\rangle$, and $|\nu, L = 1, F = 3/2\rangle$ Rydberg states, respectively. The black points correspond to experimentally observed states by microwave spectroscopy, as described in Appendix B. The gray crosses are three-photon laser spectroscopy data from Ref. [71]. The colored points denote the MQDT model bound states (the colors are chosen to guide the eye). (c),(d) Deviation between measured and modeled bound-state energies. The deviations of the laser spectroscopy measurements are divided by a factor of 20 000 and are not shown for states that were also observed by microwave spectroscopy. (e),(f) Measured (filled circles) and predicted (empty circles) $g$ factors. The gray dashed lines indicate the Landé $g$ factors in pure *LS* coupling. The error bars on the experimental data points represent the standard error from fitting the observed Zeeman shifts to Eq. (B2).

observed state energies of the $|\nu, L = 1, F = 1/2\rangle$ and $|\nu, L = 1, F = 3/2\rangle$ Rydberg states. A comparison of the experimental state energies and the MQDT model energies is presented in Lu-Fano-type plots in Figs. 4(a) and 4(b) for $F = 1/2$ and $F = 3/2$, respectively.

The behavior of the $L = 1$ states is considerably more complex than the $L = 0$ states, because the hyperfine coupling acts on states that were already strongly perturbed in $^{174}$Yb.

We observe systematic deviations between the experimental and modeled energies. The high accuracy of the microwave measurements (100 kHz) makes it clear that the deviations are systematic as opposed to random. Particularly, the dispersionlike feature in the fit residuals observed near $\nu \approx 43$ for $F = 3/2$ suggests the existence of an additional perturbing Rydberg series. The perturbing Rydberg state could come from unaccounted hyperfine splitting of excited states of the ion core or from interactions with odd-parity $L = 3$ Rydberg channels. Based on dc polarizabilities of the measured *P* Rydberg states with $\nu < 70$ and our ability to resolve Rydberg states with much larger dc polarizability, we conclude that the observed systematic deviations are not due to uncompensated stray electric fields. The significant deviations for states with $\nu < 16$ suggest an additional perturber in that energy range as well.

To confirm the accuracy of the MQDT wave functions, we also compare the predicted magnetic moments to experimental measurements [Figs. 4(e) and 4(f)]. As with the $L = 0$ series, the moments align with the Landé $g$ factors for *LS* coupling at low principal quantum number, and deviate significantly at large $\nu$ because of the combination of singlet-triplet mixing and hyperfine interaction.

We have not directly measured any $^{171}$Yb $L = 1$, $F = 5/2$ states. In *LS* coupling, this series can be described as $^3P_2(F = 5/2)$ converging to the upper $F_c = 1$ hyperfine

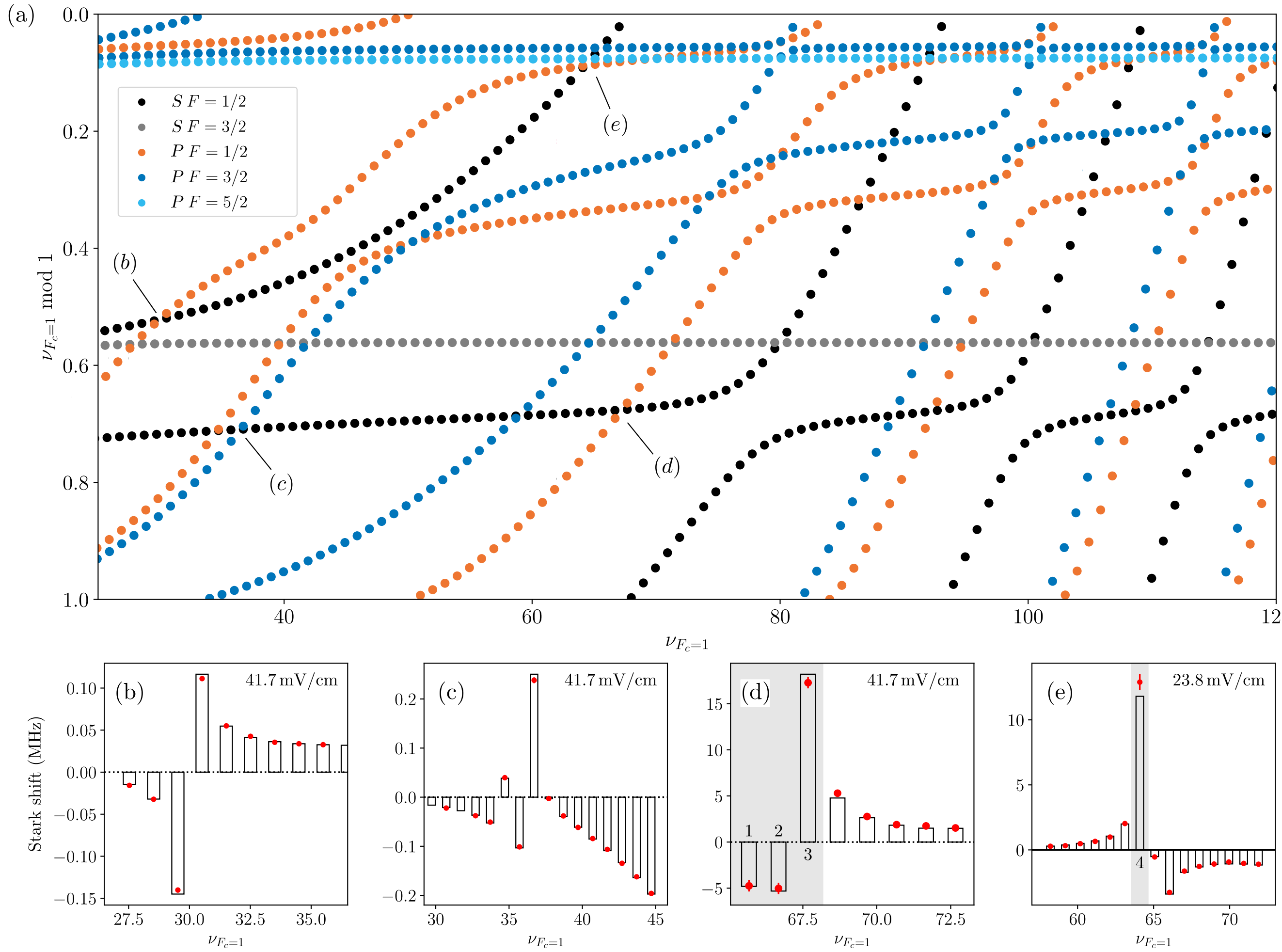

FIG. 5. (a) Combined plot summarizing the MQDT model energies for all $L=0$ and $L=1$ Rydberg series in $^{171}$Yb. (b)–(e) Measured (red) and predicted (black bars) Stark shifts of selected $L=0$, $F=1/2$ series in the vicinity of crossings with $L=1$ Rydberg series at locations indicated by markers in panel (a). The Stark shift is reported at the electric field strength indicated in each panel. The gray shaded states correspond to near degeneracies with significantly nonquadratic Stark shifts. A detailed comparison of the shifts of these states to a nonperturbative model is shown in Fig. 17. The error bars on the experimental data points in panels (b)–(e) represent the standard error from fitting the observed Stark shifts to Eq. (B1). In the case of gray shaded states, the error bars correspond to the standard error from fitting a Gaussian line profile to the Stark spectra recorded at the corresponding electric fields.

threshold. We therefore model this series using the MQDT model for the $^3P_2$ series presented for $^{174}$Yb in the previous section. To account for isotope-dependent effects, we use the MQDT model parameters as optimized from a fit to the observed $|\nu, L=1, F=3/2\rangle$ Rydberg states, which contain a contribution from the $^3P_2(F=3/2)$ states.

A summary of all measured $L=1$ state energies, Landé $g$ factors, and MQDT model parameters is presented in Supplemental Material [70].

### C. Verification of MQDT models with Stark shifts

As with $^{174}$Yb, we probe the accuracy of Rydberg state energies and matrix elements obtained from our MQDT models by measuring the dc Stark shift of the $|\nu, L=0, F=1/2\rangle$ states near degeneracies with $|\nu, L=1, F=1/2\rangle$ and $|\nu, L=1, F=3/2\rangle$ Rydberg states [Fig. 5(a)]. The measured Stark shifts are in excellent agreement with the theoretical predictions [Figs. 5(b)–5(e)] indicating good MQDT models for all relevant states, producing both accurate energies and channel contributions. Certain states with near-degenerate opposite parity states do not have quadratic Stark shifts even at very small electric fields, so we make the comparison between experiment and theory using the magnitude of the Stark shift at a particular field, instead of the usual static dipole polarizability. For these states, we also compare the measured field-dependent Stark shift with a nonperturbative calculation and find excellent agreement (Fig. 17 in Appenxdix E 1). The experimentally determined static dipole polarizabilities and Stark shifts are presented in Supplemental Material [70]. Predicted polarizability trends of the $L = 0$ Rydberg states of both $^{171}$Yb and $^{174}$Yb Rydberg states are presented in Appendix F.

## IV. RYDBERG-RYDBERG INTERACTIONS IN $^{171}$Yb

A precise understanding of the interaction potential is important to realize high-fidelity gate operations. In this section, we use the developed MQDT model to predict the interaction potential for a pair of $^{171}$Yb atoms, then validate the model using direct experimental measurements in an optical tweezer array. The calculation builds on established techniques for performing similar calculations in alkali atoms based on numerically diagonalizing the multipolar interaction Hamiltonian in a large basis of pair states [86,87]. In the context of alkali atoms, this approach has been experimentally validated by spectroscopic measurements in optical tweezers [15,16] and optical lattices [24]. We follow the formalism extending these techniques to states described by MQDT that was introduced previously in Refs. [44,52].

We first consider the interaction potential between a pair of atoms in a $|\nu, L = 0, F = 1/2, m_F\rangle$ state. For concreteness, we focus on the triplet-connected $|54.28, L = 0, F = 1/2, m_F\rangle$ states. The calculated pair potentials for the four combinations of $m_F$ sublevels is shown in Fig. 6. The predicted pair potential closely follows the expected van der Waals form $V(R) = C_6/R^6$, with $C_6 \approx h \times 34$ GHz(μm)$^6$. For comparison, we note that the $C_6$ coefficient for the $n\ ^2S_{1/2}$ state with the most similar $\nu$ ($n = 57$) is $C_6 \approx h \times 76$ GHz(μm)$^6$ [87].

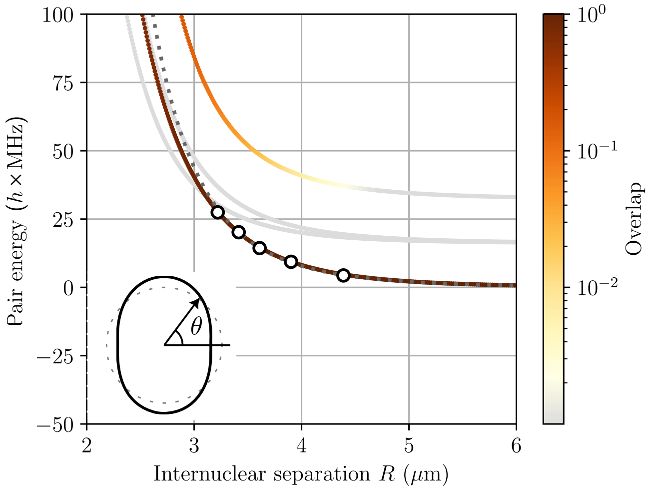

FIG. 6. Predicted pair-interaction potentials for a target Rydberg state $|t\rangle = |54.28, L = 0, F = 1/2, m_F = -1/2\rangle$ together with measured energy shifts (white circles). The magnetic field strength is 4.88(6) G corresponding to a Zeeman splitting of 16.1 MHz, and is oriented at $\theta = \pi/2$ to the interatomic axis. The color of the curves denotes the overlap of each eigenstate with the target pair state $|t\rangle^{\otimes 2}$. The gray dashed line shows the asymptotic $1/R^6$ scaling. Inset: predicted angle dependence of the $C_6$ coefficient. $\theta$ is the angle between the magnetic field and the interatomic axis.

We test the theoretical prediction by directly measuring the van der Waals shift using a pair of atoms in optical tweezers with separations from 3.3 to 4.5 μm. The measured energy shift is in excellent agreement with the predicted pair potential after scaling the experimental interatomic separation by a factor of 0.97 relative to the predicted separation (Fig. 6), which we attribute to imperfect focusing of the optical system used to project the tweezer array. Additional details about the measurement technique are described in Appendix C.

We note that there is a nearby $F = 3/2$ $D$ state with a detuning of only 68 MHz at zero magnetic field. As this state is also laser accessible from $^3P_0$, it could cause problems for blockade gates if its van der Waals interaction has the opposite sign from the target state, pushing it into resonance. We are unable to predict the $D$ state interactions because we do not yet have an MQDT model for the $F$ states. However, we note that this problem can be avoided by using the next lowest triplet-connected $S$ state with $\nu = 53.30$, where the nearest $D$ state is detuned by more than 600 MHz.

The predicted interaction strength is anisotropic, where the $C_6$ coefficient is approximately 46% larger when the internuclear axis is aligned perpendicular to the magnetic field compared to a parallel alignment to the magnetic field (Fig. 6, inset). In contrast, the van der Waals interaction between alkali atoms in $S$ states is usually highly isotropic because of the small spin-orbit coupling in the $P$ states participating in the interaction [88]. For example, the $C_6$ coefficient for the 50 $^2S_{1/2}$ state in Rb has an anisotropy of approximately 1%. The large anisotropy in this $^{171}$Yb state is attributed to the large spin-orbit coupling in Yb (scaling as $Z^4$) and series perturbers that lift the degeneracy between $J$ manifolds [as shown in Fig. 1(b) for the $^{174}$Yb $P$ series], which has the same effect as spin-orbit coupling. The anisotropy also results in off-diagonal $C_6$ interactions that mix different $m_F$ levels. As seen from the color scale in Fig. 6, the $|m_F = 1/2, m_F = 1/2\rangle$ state acquires a significant $|m_F = -1/2, m_F = -1/2\rangle$ character once the van der Waals shift becomes comparable to the Zeeman splitting. This effect is suppressed if the interatomic spacing is parallel to the magnetic field, as a consequence of the dipole-dipole selection rules [88].

We have computed the $C_6$ coefficient for all of the $F = 1/2$ series, and summarized the results in Fig. 22. The $C_6$ coefficient for the triplet-connected $F = 1/2$ series follows the expected $\nu^{11}$ scaling in the range $\nu \lesssim 65$. The singlet-connected $F = 1/2$ series has a much smaller $C_6$ coefficient in this range, with the exception of isolated states with accidental hyperfine-induced Förster resonances. This is consistent with previous estimates of a small $C_6$ for the $^{174}$Yb $^1S_0$ series using a single-channel approximation [89].

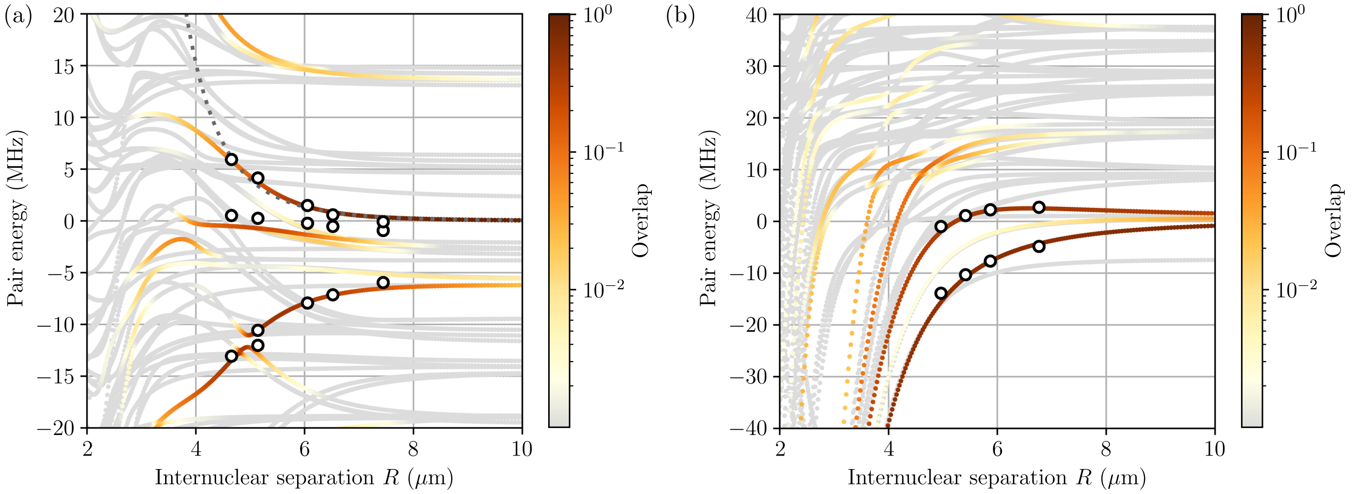

FIG. 7. Predicted pair-interaction potentials for a target state $|54.56, L = 0, F = 3/2, m_F\rangle$ with (a) $m_F = 3/2$ and (b) $m_F = -3/2$ at a magnetic field of 5.03(6) G ($\theta = \pi/2$). The color of the curves denotes the overlap with the target pair state. The white circles indicate experimentally observed resonances as described in the text. The gray dashed line in panel (a) shows the asymptotic $1/R^6$ scaling.

Next, we consider an $F = 3/2$ target state. Specifically, we consider the state $|54.56, L=0, F=3/2, m_F=+3/2\rangle$, which was used to implement two-qubit gates in Ref. [40]. The computed pair potential is shown in Fig. 7(a). Unlike the $F = 1/2$ state shown in Fig. 6, the pair potential for this $F = 3/2$ state deviates strongly from the idealized $C_6/R^6$ van der Waals scaling because of a previously unknown Förster resonance with a pair state made up of $L = 1$ states with $F = 3/2$ and $F = 5/2$. At zero magnetic field, this pair state is detuned by only approximately 3 MHz from the $|54.56, L = 0, F = 3/2\rangle^{\otimes 2}$ pair state. The complex series of crossings results from different magnetic sublevels being pushed into exact resonance by the interaction in a finite magnetic field of $B \approx 5$ G. Similar behavior is observed for the $m_F = -3/2$ states, though the resulting spectrum is slightly less complex as the Zeeman shift has the same sign as the van der Waals interaction.

We have also experimentally measured the interaction shifts for this state. We are able to identify all pair states from this complex spectrum with an overlap of more than 10% with the target state and find good agreement for both $m_F = +3/2$ and $m_F = -3/2$ using the same rescaling factor of the interatomic separation (0.97) used in Fig. 6. In the case of $m_F = +3/2$, we observe deviations of 1–2 MHz for one of the eigenstates. This is comparable in magnitude to the fit residuals in the $F = 3/2$ $P$ series MQDT model (Fig. 4; the $F = 3/2$ state that contributes to the Förster resonance is in the blue colored series in that figure).

A quantitative analysis of Rydberg interaction strengths of $S$ $F = 1/2$ and $S$ $F = 3/2$ Rydberg states is presented in Appendix G.

## V. IMPROVED TWO-QUBIT GATES

The Förster resonance observed for the $|54.56, L = 0, F = 3/2\rangle$ state is not accidental, but rather a systematic trend: Almost all $|\nu, L = 0, F = 3/2\rangle$ states with $\nu > 30$ have a Förster defect less than 10 MHz (Fig. 23). While Förster resonances are sometimes sought to increase the strength of the Rydberg-Rydberg interaction at long range [90,91], such a near-degenerate resonance is problematic for two-qubit gates because it results in a large number of weakly allowed transitions near zero energy at short separations, allowing Rydberg excitation within the blockade radius [92]. This effect is sometimes referred to as Rydberg spaghetti. At the same time, Förster resonances increase the long-range tail of the interactions, preventing parallel implementation of gates in a qubit array [93]. Understanding the existence of this Förster resonance resolves several observations from Ref. [40], including an unknown contribution to the error budget of about 1% and the need to use a large separation (43 μm) between adjacent dimers to achieve the highest gate fidelity.

We now demonstrate improved gate performance using the $|54.28, L = 0, F = 1/2\rangle$ state. Previous demonstrations of entangling gates in $^{171}$Yb used $F = 3/2$ states [31,40]. The highest reported fidelity is $\mathcal{F} = 0.980(1)$, which is approximately 1% lower than the predicted fidelity of $\mathcal{F} = 0.989$ based on error sources that were understood at the time [40]. We conjecture the additional errors were the result of unwanted Rydberg excitation to nearby pair states (Fig. 7), and that the $F = 1/2$ state with a cleaner interaction potential will lead to higher fidelity.

We implement a two-qubit gate using the same approach as Ref. [40]. Briefly, we prepare an array of four pairs of atoms (with a spacing of $d = 2.4$ μm between atoms within a pair, and $D = 24$ μm between pairs) and implement controlled-z (CZ) gates in parallel using a variant of the time-optimal two-qubit gate [94]. The gate is driven using a UV laser at 302 nm, with a power of 20 mW in a beam with a $1/e^2$ radius of 12 μm to achieve a Rabi frequency of

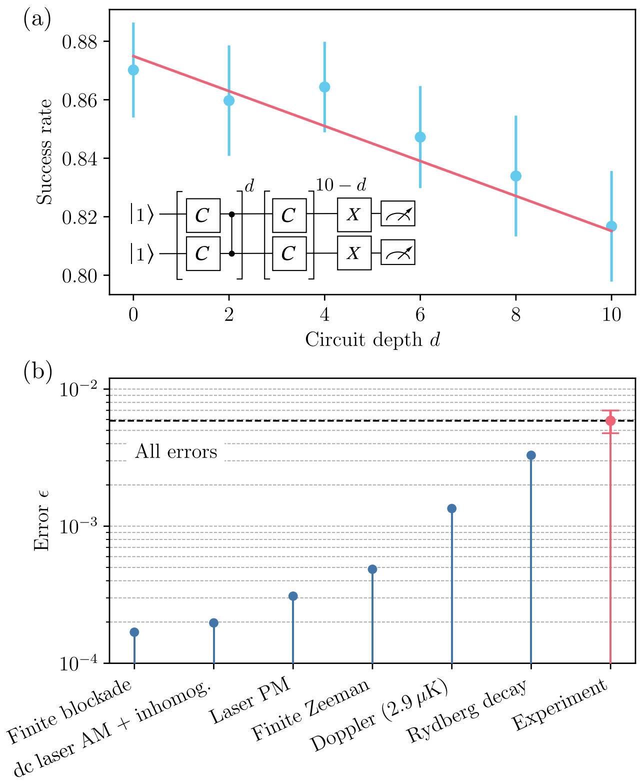

FIG. 8. (a) Randomized circuit characterization of the time-optimal cz gate using a variable depth $d$. The error bars represent the standard deviation of the measured values observed across repeated iterations of the experiment. The fitted error rate is $\epsilon = 5.6(1.1) \times 10^{-3}$ per two-qubit gate. (b) Numerical simulation of contributions to the gate error, including the finite Rydberg state lifetime, Doppler shifts from atomic motion, off-resonant excitation of neighboring $m_F$ sublevels in finite magnetic fields, shot-to-shot and site-to-site laser amplitude variations, finite Rydberg blockade, and fast laser phase noise (PM). The total simulated error rate with all sources applied simultaneously is $\epsilon = 5.9 \times 10^{-3}$ (black dashed line), in good agreement with the experimentally measured error rate (red point).

$\Omega = 2\pi \times 2.5$ MHz between $^3P_0$ $m_F = +1/2$ and a Rydberg state with $m_F = -1/2$. Because of geometric constraints, the laser is linearly polarized perpendicular to the magnetic field, such that only half of the power contributes to the $\sigma^-$ transition that drives the gate. We estimate the fidelity using the randomized circuit characterization approach of Refs. [40,95], with interleaved global single-qubit gates. With these parameters, we observe a cz gate fidelity of $\mathcal{F} = 0.994(1)$ (Fig. 8).

The randomized circuit characterization involves varying the number of two-qubit gates $d$ while keeping the number of single-qubit gates and the overall sequence duration constant. This approach allows us to isolate errors specific to two-qubit operations from other sources of error in the circuit. Each randomized circuit is designed to bring the system to the final state $|00\rangle$. As a function of the circuit depth $d$, we experimentally characterize the success rate $P_{00}$ of the circuit. The experimental success rates are fitted to an exponential decay model $P_{00} = A(1-\epsilon)^d$. Only two-qubit gate errors will contribute to $\epsilon$, while the offset at zero circuit depth $A \approx 0.87$ captures other sources of error in the circuit, including state preparation and measurement errors, and single-qubit gate errors [40,95,96].

This result improves on the previous best gate in $^{171}$Yb by a factor of 3.3. Importantly, the error budget for the gate in Fig. 8(a) is now in excellent agreement with a model based on independently measured sources of error [Fig. 8(b)] [40]. The dominant contributions are the finite lifetime of the Rydberg state [measured to be $T_r = 56(4)$ μs contributing an error of $\epsilon = 3.3 \times 10^{-3}$] and Doppler shifts ($\epsilon = 1.4 \times 10^{-3}$ at an atomic temperature during the gate of $T = 2.9$ μK). We also estimate the impact of other sources of error, including unwanted excitation of the other $m_F$ sublevel of the Rydberg state ($\epsilon = 4.8 \times 10^{-4}$), site-to-site and shot-to-shot laser intensity variation ($\epsilon = 2.0 \times 10^{-4}$), a finite Rydberg blockade strength ($\epsilon = 1.7 \times 10^{-4}$; the pulse is not compensated for the finite blockade [93,94]), and fast laser phase noise ($\epsilon_{\mathrm{PM}} = 3.1 \times 10^{-4}$). Since the dominant errors can be suppressed by increasing the gate speed (i.e., with additional laser power), these results suggest that significantly higher gate fidelities are within reach for $^{171}$Yb.

## VI. DISCUSSION AND CONCLUSION

We have presented detailed spectroscopy and modeling of the Rydberg states of both $^{174}$Yb and $^{171}$Yb with $L \leq 2$. The models are validated with experimental measurements of Stark shifts, magnetic moments, and Rydberg interactions. To the best of our knowledge, this is the most comprehensive validation of an MQDT model for a complex atom, and allows key properties for Rydberg atom quantum computing and simulation to be predicted with the level of accuracy that is routine for alkali atoms. This will provide vital input for future experiments in quantum computing and simulation with Yb or with Yb-alkali mixtures. Moreover, the calculation technique is a template for exploring other atoms in the lanthanide group, such as Ho or Er [64,65].

We used this model to identify the likely cause of previously unattributed errors in entangling gates using $F = 3/2$ Rydberg states. We also predicted a more suitable Rydberg state with $F = 1/2$, leading to an improved gate fidelity of $\mathcal{F} = 0.994(1)$, with errors reduced by a factor of 3.3 compared to the previous best gate demonstration using $^{171}$Yb [40].

We identify several avenues for future work. The first is including states with $L \geq 3$, which are needed to accurately predict the interactions of $D$ states, which can create blockade violations for $S$ states. The second is to extend the model to predict Rydberg state lifetimes and decay branching ratios, which will involve more careful fitting of

MQDT models to low-$n$ perturbers and including matrix elements between different core electron states [43]. While low-$n$ perturbers have little effect on the Rydberg character of high-$n$ states, they can have a large impact on the lifetime and decay branching ratio by providing a new decay pathway via the population of the perturbing state [20,43].

Another area of interest is the behavior of autoionizing states of the form $6p_{1/2}n\ell$. These states have found use for Rydberg atom detection [97,98], coherent control [99,100], and in quantum error correction [39]. To our knowledge, only the $^{174}$Yb $^3S_1$ autoionizing series has been characterized [99]. A systematic study, including $^{171}$Yb, would be beneficial for applications relying on use of these states.

Finally, we note that these models may have applications beyond quantum computing. Ytterbium clocks are among the most precise in the world [101], and Rydberg states can be used for generating entanglement to enhance precision [35,36]. It has also been proposed to use Rydberg states for *in situ* absolute calibration of the temperature through the blackbody radiation spectrum [102], which would warrant more precise validation of the modeled matrix elements.

## ACKNOWLEDGMENTS

We gratefully acknowledge helpful conversations with Adam Kaufman and Aruku Senoo, and Professor Herbert Rinneberg for providing a copy of Ref. [71]. This work was supported by the Army Research Office (Grant No. W911NF-1810215), the Office of Naval Research (Grant No. N00014-20-1-2426), DARPA ONISQ (Grant No. W911NF-20-10021), the National Science Foundation (QLCI Grant No. OMA-2120757, and NSF CAREER Grant No. PHY-2047620), the Sloan Foundation, and the Gordon and Betty Moore Foundation (Grant No. GBMF12253).

## APPENDIX A: MQDT FORMALISM

Energies and wave functions of Rydberg states are crucial for evaluating state properties (e.g., Stark shifts [12]). Several open-source programs have been developed for nonperturbative calculations of Stark shifts and interaction potentials for alkali metal atoms [86,87] or alkaline-earth atoms within a single-channel quantum defect approximation [45]. However, for divalent atoms, an MQDT treatment is necessary to obtain accurate Rydberg state energies and wave functions.

MQDT was introduced by Seaton [41] and reformulated with the concept of frame transformations by Fano [42] and is established as a powerful framework for analyzing the Rydberg states of atoms [43,62,64,65,77,83,103–109] and molecules [42,110,111] with low-lying core-excited states.

Calculations based on MQDT models predicting dc polarizabilities and Rydberg-Rydberg interaction for complex atoms have been presented previously [44,52,68], but the conceptual complexity and lack of comprehensive MQDT characterization of atomic species has limited the broad adoption of this approach.

This appendix is intended to serve as a comprehensive introduction and overview to this approach, which will be useful beyond the specific case of Yb atoms. We have also made the software used to perform the computations in this work available as an open-source package RYDCALC [112].

### 1. MQDT model

MQDT treats the short- and long-range interactions of a single active electron with different configurations of the ion core. Each unique combination of angular quantum numbers of the electron–ion-core system is referred to as a channel. When the active electron is far away from the ion core, the system is well described by “collision” channels indexed by $i$. In this region, the interaction between the ion core and the active electron is dominated by the Coulomb interaction, and the system is appropriately described in $jj$ coupling.

The energy $E$ can be expressed with respect to the ionization limit of the $i$th collision channel $I_i$ as

$$E = I_i - (hcR_M)/\nu_i^2, \tag{A1}$$

where $\nu_i$ is the effective principal quantum number with respect to $I_i$, and $R_M = R_\infty(1 - m_e/M)$ is the mass-reduced Rydberg constant, where $m_e$ is the mass of the electron and $M$ is the atomic mass.

When the active electron is close to the ion core, their interaction is dominated by non-Coulombic electrostatic interactions. Channels describing the angular momentum coupling (typically $LS$ coupling) in this regime more appropriately are called “close-coupling” channels indexed by $\alpha$. In this region, scattering between the electron and the ion core mixes $i$ channels with the same total angular momentum $J$ (or $F$ in the presence of a nonzero nuclear spin) and parity. The wave function of channel $i$ can therefore be expressed as a superposition of $\alpha$ channel wave functions with amplitude $\tilde{A}_\alpha$. At large electron–ion-core separations, the wave function at energy $E$ can be written as [62]

$$|\Psi\rangle = \sum_i |\Phi_i\rangle \bigg[ f(\nu_i, r) \sum_\alpha U_{i\alpha} \cos(\pi\mu_\alpha)\tilde{A}_\alpha - g(\nu_i, r) \sum_\alpha U_{i\alpha} \sin(\pi\mu_\alpha)\tilde{A}_\alpha \bigg], \tag{A2}$$

where the terms in the square brackets correspond to the radial part of the active electron’s wave function, and the spin and orbital angular momentum couplings of the outer electron and the ion-core wave function are given by $|\Phi_i\rangle$. $f(\nu_i, r)$ and $g(\nu_i, r)$ correspond to the regular and irregular Coulomb wave functions [42]. The short-range, non-Coulombic interaction of the Rydberg electron and the ion core are encoded in eigenchannel quantum defects $\mu_\alpha$, and the channels are coupled by the unitary transformation matrix $U_{i\alpha}$.

For discrete bound states, the wave function Eq. (A2) must remain finite at large separation, resulting in the boundary condition [42,62]

$$\sum_\alpha \tilde{A}_\alpha U_{i\alpha} \sin[\pi(\nu_i + \mu_\alpha)] = 0. \tag{A3}$$

This gives nontrivial solutions for the bound-state energies $\nu_i$ when $\det|F_{i\alpha}| = 0$ is zero, where $F_{i\alpha}$ is given by

$$F_{i\alpha} = U_{i\alpha} \sin[\pi(\mu_\alpha + \nu_i)]. \tag{A4}$$

Bound states are found at the intersection of the surface spanned by Eq. (A4) and the curve:

$$\nu_i = \left(\frac{I_i - I_j}{R_M} + \frac{1}{\nu_j^2}\right)^{-1/2}, \tag{A5}$$

where $\nu_i$ and $\nu_j$ are effective principal quantum numbers relative to the $i$th and $j$th ionization limit $I_i$ and $I_j$, respectively.

The MQDT model is fully specified by the unitary transformation matrix $U_{i\alpha}$ and the eigenchannel quantum defects $\mu_\alpha$. The task in determining accurate MQDT models therefore reduces to finding values of $U_{i\alpha}$ and $\mu_\alpha$, which reproduce experimental observables such as state energies, Landé $g$ factors, or dc polarizabilities.

### 2. MQDT model parameters

The transformation matrix $U_{i\alpha}$ is orthogonal and can therefore be constructed from at most $N(N-1)/2$ rotation matrices, in the case of an $N$-channel model [103]. In practice, the mixing between channels is small, and a suitable approximation can be made by composing significantly fewer rotation matrices. As noted above, the natural basis at long range is $jj$ coupled, while at short range it is $LS$ coupled. We can therefore simplify $U_{i\alpha}$ by introducing an intermediate basis $\bar{\alpha}$ of purely $LS$-coupled channels, and writing $U_{i\alpha}$ as the product of the $jj$-$LS$ transformation matrix $U_{i\bar{\alpha}}$ and a second matrix $V_{\bar{\alpha}\alpha}$ representing mixing between $LS$-coupled channels [103,113]:

$$U_{i\alpha} = U_{i\bar{\alpha}} V_{\bar{\alpha}\alpha}, \tag{A6}$$

where $U_{i\bar{\alpha}}$ corresponds to the $LS$-$jj$ frame transformation

$$\begin{aligned} U_{i\bar{\alpha}} &= \langle [(S_c L_c) J_c (s\ell) j] J | [(S_c s) S (L_c \ell) L] J \rangle \\ &= [S, L, J_c, j]^{1/2} \begin{Bmatrix} S_c & L_c & J_c \\ s & \ell & j \\ S & L & J \end{Bmatrix} \end{aligned} \tag{A7}$$

from Eq. (6.4.2) of Ref. [114] and $[a, b, \ldots]^{1/2} = \sqrt{(2a+1)(2b+1)\ldots}$.

The second matrix $V_{\bar{\alpha}\alpha}$ accounts for configuration interaction by introducing couplings between the $\bar{\alpha}$ channels. $V_{\bar{\alpha}\alpha}$ is typically expressed as a series of rotations by Euler angles $\theta_{ij}$ around channels $i$ and $j$ [see Eq. (15) of Ref. [115]]

$$V_{\bar{\alpha}\alpha} = \prod \mathcal{R}(\theta_{ij}). \tag{A8}$$

If the $\theta_{ij}$ are small, the sequence of the rotations in Eq. (A8) is not critical; however, in general, $U_{i\alpha}$ will be sensitive to the chosen order.

In general, even in the absence of multichannel interactions, the eigenchannel quantum defect is energy dependent. The energy dependence originates, for example, from a polarization of the ion core by the outer electron [116]. In practice, the eigenchannel quantum defect slowly varies only with energy, and we treat the energy dependence of the eigenchannel quantum defects as

$$\mu_\alpha(\epsilon) = \mu_\alpha^{(0)} + \epsilon \mu_\alpha^{(2)} + \epsilon^2 \mu_\alpha^{(4)} \ldots, \tag{A9}$$

and similarly, we treat the energy dependence of $\theta_{ij}$ by

$$\theta_{ij}(\epsilon) = \theta_{ij}^{(0)} + \epsilon \theta_{ij}^{(2)} \ldots, \tag{A10}$$

where $\epsilon = 1/\nu^2$ [103].

### 3. MQDT models for hyperfine isotopes

For isotopes with nonzero nuclear spin, the hyperfine interaction in the ion core has to be considered. Here, we follow a similar formalism introduced in earlier work [77,81,82].

In the close-coupling region, the hyperfine interaction in the ion core is small compared to the exchange interaction and can be treated as perturbation to the fine structure. The close-coupling $\alpha$ channels are split into $\alpha_F = |\{[(S_c s) S (L_c \ell) L] J I\} F\rangle$ channels, where the MQDT parameters $\mu_\alpha \approx \mu_{\alpha_F}$ and $U_{i\alpha} \approx U_{i\alpha_F}$ are only slightly affected. Therefore, we can construct the MQDT models for isotopes with nonzero nuclear spin from MQDT models obtained from even isotopes with nuclear spin $I = 0$. In this work, we use the MQDT models and parameters obtained for $^{174}$Yb and introduce hyperfine coupling of the ion core with

$$U_{i_F,\alpha_F} = U_{i_F,i} U_{i,\alpha_F}, \tag{A11}$$

where

$$U_{i,\alpha_F} = U_{i\bar{\alpha}} V_{\bar{\alpha}\alpha_F}, \tag{A12}$$

and $U_{i_F,i}$ is the frame transformation

$$U_{i_F,i} = \langle\{[(J_cI)F_cj]F|(J_cj)JI\}F\rangle = (-1)^{I+j+F_c+J}[J,F_c]^{1/2}\begin{Bmatrix} I & J_c & F_c \\ j & F & J \end{Bmatrix}, \qquad \text{(A13)}$$

where $J$ corresponds to the total electronic angular momentum, $I$ is the nuclear spin, $F$ is the total angular momentum including nuclear spin, which uses Eq. (6.4.2) of Ref. [114].

We find that directly applying the $^{174}$Yb MQDT parameters (i.e., eigenchannel quantum defects $\mu_\alpha$ and rotations $\theta_{ij}$) to the $^{171}$Yb energies generally gives good agreement, but we find that a slight reoptimization of the model parameters is necessary for an improved modeling. We attribute this variation to three main reasons. First, a small isotope dependence [52] and hyperfine-induced mixing of channels can yield variations in the close-coupling parameters. Second, while we do not explicitly include direct coupling of the outer electron with the nucleus, this interaction can be expressed through the matrix elements of $V_{\bar{\alpha}\alpha}$ and $\mu_\alpha$. Therefore, to the extent that this interaction is significant, it can be incorporated into the model. We note that the magnitude of this direct coupling scales as $\nu^{-3}$ [69] and is at the scale of 1 MHz at $\nu = 30$, which is smaller than the current disagreement between the MQDT model and the experimentally measured state energies (i.e., Fig. 4). Therefore, attempting to predict this interaction strength and including it by hand would not significantly improve the model prediction. Third, we consider only the hyperfine splitting in the $6s\,^2S_{1/2}$ ground state of the $^{171}$Yb$^+$ ion. We neglect the hyperfine splitting of excited states of the $^{171}$Yb$^+$-ion core. This is likely a good approximation because the excited states are energetically far above the channels converging to the $^{171}$Yb$^+$ ground state considered in this work, but could lead to changes in the MQDT parameters.

### 4. MQDT wave functions

Once a bound state $b$ has been found with Eqs. (A4) and (A5), its wave functions are conveniently expressed in the $jj$ basis, and Eq. (A2) is rewritten as

$$|\psi_b\rangle = |\Psi_b\rangle/N_b = \sum_i |\Phi_i\rangle P_{\nu_{i,b},\ell_i}(r)A_{i,b}, \qquad \text{(A14)}$$

where $P_{\nu_{i,b},\ell_i}(r)$ is the radial Coulomb function of the active electron, $A_{i,b}$ are the normalized channel contributions in terms of collision channels $i$ in $jj$ coupling [103]

$$A_{i,b} = (-1)^{l_i+1}(\nu_{i,b})^{3/2}\sum_\alpha U_{i\alpha}\cos[\pi(\nu_{i,b}+\mu_\alpha)]\tilde{A}_{\alpha,b}/N_b, \qquad \text{(A15)}$$

and $N_b$ ensures the normalization [41] of the wave function and is given by [103]

$$N_b^2 = \sum_{i,\alpha}\nu_{i,b}^3 U_{i\alpha}\cos[\pi(\nu_{i,b}+\mu_\alpha)]\tilde{A}_{\alpha,b} + \sum_\alpha\left(\frac{\mathrm{d}\mu_\alpha}{\mathrm{d}E}\right)\tilde{A}_{\alpha,b}^2 + \frac{1}{\pi}\sum_{i,\alpha,\beta}\left(\frac{\mathrm{d}U_{i,\alpha}}{\mathrm{d}E}\right)U_{i,\beta}\sin[\pi(\mu_\alpha-\mu_\beta)]\tilde{A}_{\alpha,b}\tilde{A}_{\beta,b}. \qquad \text{(A16)}$$

The wave-function coefficients $\tilde{A}_{\alpha,b}$ of Eq. (A2) are obtained by evaluating

$$\tilde{A}_{\alpha,b} = C_{i\alpha}\Big/\left[\sum\nolimits_\alpha C_{i\alpha}^2\right]^{1/2}, \qquad \text{(A17)}$$

where $C_{i\alpha}$ is the cofactor of the $i$th row and $\alpha$th column of the matrix $F_{i\alpha}$ [see Eq. (A4)], and in the evaluation of Eq. (A17), channel $i$ can be chosen for convenience [103].

The close-coupling $\alpha$ channel fractions ($LS$ coupling) can be obtained from $A_i$ as

$$A_{\bar{\alpha},b} = \sum_i U_{i\bar{\alpha}}A_{i,b}. \qquad \text{(A18)}$$

### 5. Evaluation of matrix elements

We evaluate the matrix elements following the procedures introduced in Ref. [44], which are summarized in the following.

Single-atom matrix elements between states $b$ and $b'$ of operator $\hat{\zeta}$ acting on the channel function $|\Phi_i\rangle$ in Eq. (A14) that leaving the orbital angular momentum $l$ of the Rydberg electron unchanged are evaluated by

$$\zeta_{b,b'} = \sum_{i,i'}(A^T)_{b,i}\,\langle\Phi_i|\hat{\zeta}|\Phi_{i'}\rangle O_{ib,i'b'}A_{i',b'}, \qquad \text{(A19)}$$

where

$$O_{ib,i'b'} = \int_0^\infty P_{\nu_{i,b},\ell_i}(r)P_{\nu_{i',b'},\ell_{i'}}(r)dr \qquad \text{(A20)}$$

is a radial overlap integral. The overlap integral can either be evaluated using analytic approximations [44,117] or numerical wave functions obtained from the Numerov algorithm [12,117].

This form of matrix elements is used in the evaluation of magnetic moments in the paramagnetic interaction Hamiltonian

$$H_{\mathrm{PM}} = -\vec{\mu}\cdot\vec{B} = \{\mu_B[\vec{L}_c + \vec{\ell} + g_s(\vec{S}_c + \vec{s})] - \mu_I\vec{I}\}\cdot\vec{B} \qquad \text{(A21)}$$

using the expressions presented in Ref. [44] for the general case of Rydberg states with hyperfine interaction in the ion core, where $\mu_B$ is the Bohr magneton, $\mu_I$ is the nuclear magnetic moment, and $g_s$ is the electron spin $g$ factor.

For the case of the multipole operator $\hat{\mathcal{Q}}^{(kq)} = r^k Y_{k,q}(\Omega)$, the contribution of the core electrons is neglected, and only the contribution of the Rydberg electron is considered (because of its much larger spatial extent):

$$\mathcal{Q}^{(kq)}_{b,b'} = \sum_{i,i'} (A^T)_{b,i} \langle \Phi_i | Y_{kq} | \Phi_{i'} \rangle R^{(k)}_{ib,i'b'} A_{i',b'}, \tag{A22}$$

where $R^{(k)}_{ib,i'b'}$ is the radial integral

$$R^{(k)}_{ib,i'b'} = \int r^k P_{\nu_{i,b},\ell_i}(r) P_{\nu_{i',b'},\ell_{i'}}(r) dr. \tag{A23}$$

Matrix elements of the form presented in Eq. (A22) are used in the calculation of Stark shifts [12], Rydberg-Rydberg interactions [14], and the diamagnetic shift.

The diamagnetic interaction Hamiltonian [118] is given by

$$H_{\mathrm{DM}} = \frac{1}{8m_e} |\vec{d} \times \vec{B}|^2, \tag{A24}$$

and can be expressed in terms of spherical harmonics (compare, e.g., Ref. [86])

$$H_{\mathrm{DM}} = \frac{e^2}{12m_e} r^2 \sqrt{4\pi} \left( Y_{0,0} - \sqrt{\frac{1}{5}} Y_{2,0} \right) B^2. \tag{A25}$$

Because of the multichannel nature of MQDT eigenstates, calculating matrix elements between two MQDT eigenstates as presented in Eqs. (A19) and (A22) requires calculating radial and angular integrals for all combinations of the electronic configurations encoded in the channel wave functions. We note that if a state has contributions from channels with significantly different ionization limits, the radial Coulomb functions $P_{\nu_{i,b},\ell_i}(r)$ of each channel will vary significantly in spatial extent because of the $\nu^2_{i,b}$ scaling of the orbital radius of the active electron. In practice, we neglect the contribution of channels with ionization limits significantly larger than the first ionization limit, since the associated wave functions are much more compact than those belonging to the lower limit and have comparatively small contributions to matrix elements of the form $r^k$. The only case in which radial wave functions corresponding to different thresholds are considered is in the case of the hyperfine-split thresholds in $^{171}$Yb.

### 6. Numerical evaluation

We compute state polarizabilities and interaction potentials following numerical techniques established for alkali atoms [12,86,87,119] but adapted to compute matrix elements of MQDT eigenstates as described in the previous section. We review the approach here to highlight the important features.

The energy of an atom in electric and magnetic fields $F$ and $B$ is given by

$$H = H_0 + Fer + H_{\mathrm{PM}} + H_{\mathrm{DM}}, \tag{A26}$$

where $H_0$ encodes the energy in the absence of the field, and $H_{\mathrm{PM}}$ and $H_{\mathrm{DM}}$ are defined in Eqs. (A21) and (A24), respectively. To determine the energy shift for a target state $|\psi_0\rangle$, we numerically evaluate the matrix elements of Eq. (A26) in a large basis of states $\{|\psi_i\rangle\}$, and then diagonalize [12].

The matrix elements $\langle \psi_i | r | \psi'_i \rangle$ and $\langle \psi_i | r^2 | \psi'_i \rangle$ (in $H_{\mathrm{DM}}$) are evaluated using Eq. (A22). Computing the radial integral in Eq. (A23) requires numerical wave functions, which we compute using the Numerov method [12], following the implementation in the Alkali Rydberg Calculator [87]. The Numerov method computes the radial wave function of a bound state from its energy, relative to the ionization limit. We note that MQDT states do not have a unique radial wave function: Each channel may have a distinct ionization limit. Therefore, the matrix element in Eq. (A22) involves summing over several different wave functions.

The energy shift in small magnetic fields can be estimated from the diagonal elements of Eq. (A26). The Stark shift in a small electric field can be estimated from diagonalizing Eq. (A26) in a small basis consisting of the several closest states with opposite parity. However, evaluating a full Stark map with multiple level crossings, or evaluating the diamagnetic shift in large fields resulting in level crossings, requires a larger basis of hundreds or thousands of states.

The Hamiltonian of two interacting Rydberg atoms in the Born-Oppenheimer approximation can be written as

$$H = H^{(1)} + H^{(2)} + H_{\mathrm{int}}, \tag{A27}$$

where $H^{(1)}$ and $H^{(2)}$ are the Hamiltonians of the two isolated Rydberg atoms [Eq. (A26)]. The interaction Hamiltonian $H_{\mathrm{int}}$ is evaluated through an expansion over multipole terms $k_1$ and $k_2$ [120,121]

$$\begin{aligned} H_{\mathrm{int}} = {} & \sum_{k_1,k_2}^{\infty} \frac{(-1)^{k_2}}{R^{k_1+k_2+1}} \sqrt{\frac{(4\pi)^3 (2k_1+2k_2)!}{(2k_1+1)!(2k_2+1)!(2k_1+2k_2+1)}} \\ & \times \sum_{p=-(k_1+k_2)}^{k_1+k_2} \sum_{p_1=-k_1}^{k_1} \sum_{p_2=-k_2}^{k_2} C^{k_1+k_2,p}_{k_1,p_1,k_2,p_2} r_1^{k_1} r_2^{k_2} Y_{k_1,p_1}(\hat{r}_1) Y_{k_2,p_2}(\hat{r}_2) Y_{k_1+k_2,p}(\hat{R}), \end{aligned} \tag{A28}$$

where $\hat{R}$ is a vector representing the internuclear axis, $C^{k_1+k_2,p}_{k_1,p_1,k_2,p_2} = \langle k_1, p_1; k_2, p_2 | k_1 + k_2, p\rangle$ is a Clebsch-Gordan coefficient, and $Y_{\kappa,p}(\hat{r})$ are unit-normalized spherical harmonics.

The calculations presented in this work are restricted to dipole-dipole interactions ($k_1 = k_2 = 1$), though we note that higher-order multipoles can become important at short separations [24], and the $R^{-5}$ term from $k_1 = k_2 = 1$ can also dominate the asymptotically long-range interaction [89].

As with the case of the field shift, the matrix elements are evaluated numerically using Eq. (A22) at fixed internuclear separations $R$. The size of the required basis for computing pair interactions is much larger than for evaluating single-atom energy-level shifts. Moreover, compared to alkali atoms, $^{174}$Yb has twice the number of Rydberg states ($S = 0$ and $S = 1$), while $^{171}$Yb has 4 times as many when including the nuclear spin.

We therefore restrict the size of the Rydberg-pair basis by including only pair states with significant contribution to the interaction potential in an energy range close to a target pair state [14]. The Rydberg-pair basis is formed in two steps. First, we build the pair basis from a set of single-atom states with similar effective principal quantum number $\nu$ and orbital angular momentum $L$ as the target state. The resulting pair basis is then further truncated to pair states with a small pair-energy defect $\Delta E$ to the target pair state. Depending on the orientation of the internuclear axis with respect to external fields and the included orders of the multipole expansion, the basis size can be additionally restricted by making use of selection rules of the spherical harmonics under the conservation of certain symmetries [86].

$\Delta E$, $\Delta\nu$, and $\Delta L$ are then increased until convergence is observed. Typically, values of $\Delta\nu \lesssim 3$ are sufficient to produce accurate interaction potentials [14,86]. To give a sense of scale, the computations in Fig. 7 included the Rydberg-pair state with $\Delta\nu < 3$, $\Delta L = 1$, and $\Delta E < 10$ GHz, yielding a basis of approximately 2000 pair states.

## APPENDIX B: ATOMIC BEAM SPECTROSCOPY APPARATUS

The spectroscopic data presented in this article are obtained by laser and radio-frequency (rf) spectroscopy on an atomic beam of $^{174}$Yb or $^{171}$Yb atoms [see Figs. 9(a) and 9(b)]. The atomic beam is generated by heating a sample of ytterbium to a temperature of 310 °C in an oven with a collimator opening of approximately 1 cm. The atomic beam is further collimated by a pinhole with a diameter of 3 mm, approximately 12 cm after the oven collimator and 9 cm before the spectroscopy region.

Transitions to $S$ and $D$ Rydberg states are driven by a two-photon laser transition through the intermediate $6s6p\,^1P_1$ state. The laser light needed for the transition with wavelengths of 399 nm ($6s^2\,^1S_0 \rightarrow 6s6p\,^1P_1$) and 394–399 nm ($6s6p\,^1P_1 \rightarrow$ Rydberg state) is generated by frequency doubling the output of tunable titanium-sapphire (Ti:sapphire) lasers in a resonantly enhanced frequency-doubling cavity. The isotope shifts on the $6s^2\,^1S_0 \rightarrow 6s6p\,^1P_1$ transition [122] are used for an isotope selective excitation into the Rydberg state. To minimize Doppler shifts on the two-photon laser transitions, counterpropagating laser beams are applied at a 90° angle relative to the atomic beam (along the $y$ axis in Fig. 9). Laser pulses with length of $1 - 3$ μs are generated by acousto-optic modulators. The laser frequencies are monitored by measuring the frequency of the fundamental output of the Ti:sapphire laser using a HighFinesse WS8-10 wavelength meter with a specified $3\sigma$ uncertainty of 10 MHz. At regular intervals, the wavelength meter is calibrated to a 399-nm laser that is frequency locked to a ultralow-expansion cavity with known offset from the $^1S_0 \rightarrow {}^1P_1(F = 3/2)$ transition in $^{171}$Yb.

The population in Rydberg states is detected by state-selective pulsed-field ionization (see, e.g., Ref. [69]). High-voltage (HV) ramps with a maximum voltage of 2.5 kV are generated by switching between a low-voltage (during Rydberg spectroscopy) and an HV input using HV MOSFET switches (Behlke HTS 31-03-GSM) and are applied to a set of electrodes (on the right side of the atomic beam in Fig. 9) through an $RC$ low-pass filter ($\tau = 1$ μs). The resulting maximum field of approximately 833 V cm$^{-1}$ limits the lowest detectable Rydberg states in our setup to an effective principal quantum number $\nu \approx 26$. The resulting Yb$^+$ ions are accelerated toward and detected on a time-resolved microchannel-plate (MCP) ion detector (Hamamatsu F13446-11) and recorded on an oscilloscope. To reduce electric field inhomogeneities caused by the high voltage (typically $-1.9$ kV) applied to the front surface of the MCP, we place a grounded grid mesh about halfway in between the spectroscopy region and the MCP. The experiment is operated at a repetition rate of 1 kHz, limited by the current drawn at the HV supply generating the HV field-ionization ramps.

An exemplary laser spectrum of the $|40.70, S, F = 1/2\rangle$ Rydberg state of $^{171}$Yb is presented in Fig. 9(c). Transition frequencies to the Rydberg state are determined by a least-squares fit of the data to a Gaussian line-shape model.

Transition between Rydberg states are driven using rf with frequencies in the range of 10–175 GHz. The rf radiation is obtained from a Windfreak Techn., LLC SynthHD PRO (up to 24 GHz) dual-channel microwave generator or by using a combination of active ×4 (Marki Microwave AQA-2156, 21–56 GHz, 20 dBm) and/or passive ×4 (Marki Microwave MMQ-40125H, 40–175 GHz, 0 dBm) frequency multipliers. The microwave generator is referenced to a stable 10-MHz reference signal obtained from a Global-Positioning-System-disciplined Rb atomic clock (Stanford Research Systems FS725). rf pulses with duration of 1–8 μs

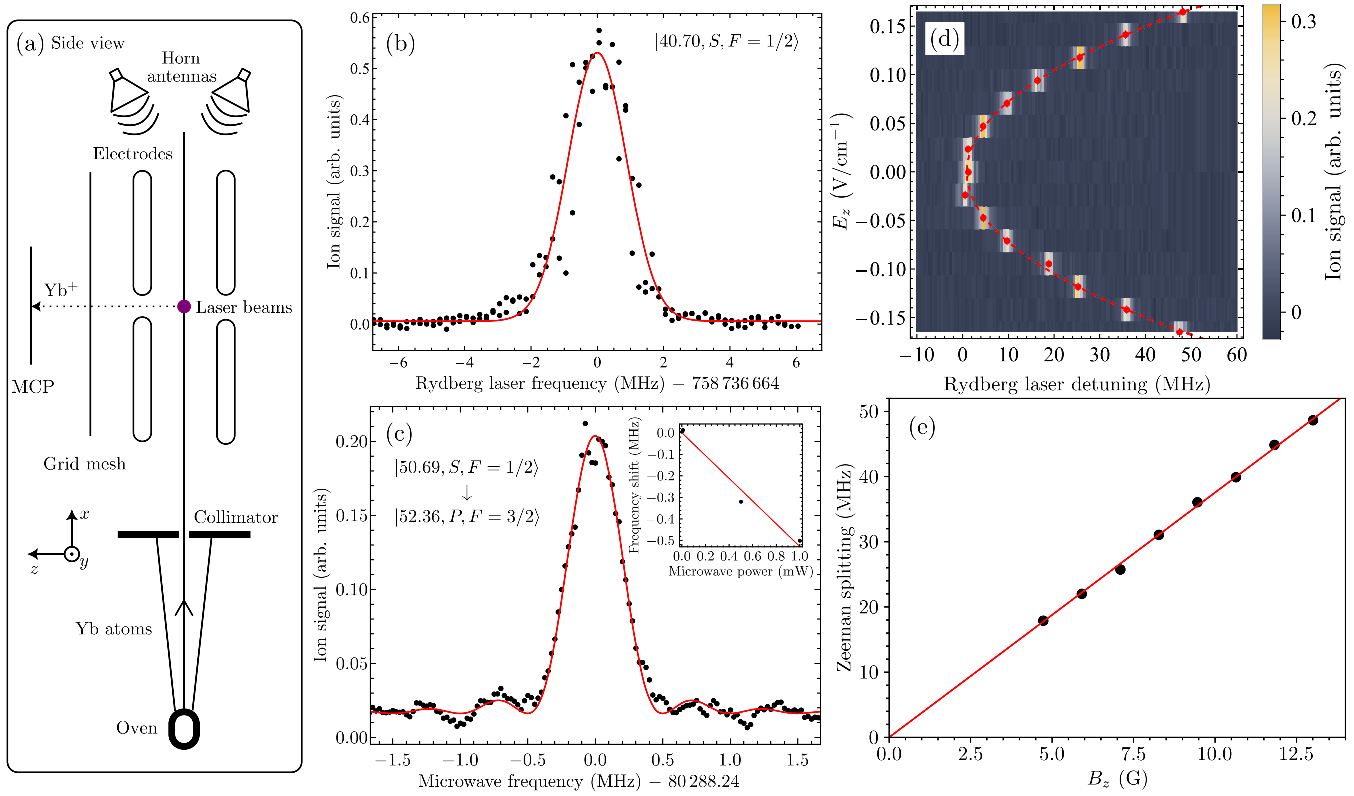

FIG. 9. (a) Schematic of the atomic beam apparatus used for spectroscopy on Yb Rydberg state. See text for details. (b) Typical laser excitation spectrum showing the $^{171}$Yb, $|40.70, S, F = 1/2\rangle$ Rydberg state. Each black point corresponds to the integrated time-resolved ion signal averaged over 1000 repetitions of the experiment. The obtained data are fit to a Gaussian line-shape model (red line) with a full width at half maximum of 2.1 MHz. (c) Typical microwave spectrum of a $|50.69, S, F = 1/2\rangle \rightarrow |52.36, P, 3 = 1/2\rangle$ transition in $^{171}$Yb. Each black point corresponds to the integrated time-resolved ion signal averaged over 1000 repetitions of the experiment. The obtained data are fit to a sinc$^2$ line-shape model (red line) for a $2 - \mu$s rectangular microwave pulse. Inset: extrapolation of the transition frequency to zero microwave power. (d) Typical polarizability measurement of the $|62.14, S, F = 1/2\rangle$ Rydberg state obtained by recording laser spectra in a range of electric fields $F_z$. The transition frequencies (red dots) are obtained by a least-squares fit of a Gaussian line-shape model to the experimental data. The static dipole polarizability of the state is obtained by a least-squared fit of Eq. (B1) (dashed red line) to observed Stark shifts. (e) Zeeman splittings between the $|50.69, S, F = 1/2, m_F = \pm 1/2\rangle$ magnetic sublevels obtained by laser spectroscopy in a magnetic field $B_z$. $g$ factors of the Rydberg states are obtained by a least-squares fit of the experimental data to Eq. (B2).

are obtained by amplitude modulating the output of the microwave generator before frequency multiplication using absorptive modulators (Hewlett Packard 33008C or 11720A). The obtained rf radiation is coupled into the vacuum chamber through vacuum viewports using suitable horn antennas. All laser radiation is switched off for the duration of the rf pulses. The power of the rf radiation is controlled using either a digital step attenuator (Analog Devices ADRF5740) or a WR-10 direct-reading attenuator (Mi-Wave 510W/387). A microwave spectrum of the $33\,^1S_0 \rightarrow 33\,^1P_1$ transition in $^{174}$Yb is presented in Fig. 9(d). Transition frequencies between Rydberg states are determined by a least-squares fit of the data to either a sinc$^2$ or Lorentzian line-shape model. All stated Rydberg-Rydberg transitions have been measured at varying rf powers and extrapolated to "zero" rf power to remove frequency shifts caused by ac Stark shifts.

To control the electric field in the spectroscopy region, we apply voltages to two segmented circular electrodes (four segments each) separated by 3 cm. Stray electric fields are compensated at the beginning of each day by minimizing the quadratic Stark shift of the $6s130s\ 130\,^1S_0$ Rydberg state of $^{174}$Yb. We observe day-to-day fluctuations of the required electric compensation fields of less than 3 mV/cm.

We determine values for the static dipole polarizabilities $\alpha_0$ of Rydberg states by measuring a shift in the transition frequencies caused by applying electric fields $F$ between the two segmented circular electrodes and subsequent fitting to

$$\Delta E_{\text{Stark}} = -(1/2)\alpha_0 F^2. \tag{B1}$$

When possible, we ensured that the static dipole polarizabilities were determined in a range of quadratic

Stark shifts. For some cases, the Stark shift deviates from a quadratic scaling even at very small electric fields, and we report values for the Stark shift at a given electric field instead.

Magnetic fields in all three spatial directions are controlled by three pairs of coils placed outside the vacuum chamber, arranged in Helmholtz configuration. The magnetic fields generated by the coils are calibrated by rf spectroscopy of the Zeeman splittings on an $n'\,^3S_1 \leftarrow n\,^1S_0$ transition, and assuming a $g$ factor of the mostly unperturbed $n^3S_1$ Rydberg series to be $g(^3S_1) = g_s \approx 2.0023$. We obtain values for Landé $g$ factors of Rydberg states by measuring Zeeman shifts caused by applying calibrated magnetic fields $B$ and a subsequent linear fit to

$$\Delta E_{\mathrm{Zeeman}} = m g \mu_B B, \tag{B2}$$

where we measured the Zeeman shifts at sufficiently small magnetic fields to avoid the effect of nonlinear diamagnetic shifts.

## APPENDIX C: MEASURING RYDBERG INTERACTIONS IN OPTICAL TWEEZERS

We measure the distance-dependent interactions between single $^{171}$Yb Rydberg atoms trapped in optical tweezer arrays using the setup described in Ref. [40]. Similar approaches have been previously used to measure $C_6$ coefficients of Rydberg-pair states in Rb [15] and angle-dependent dipole-dipole interaction strengths [16]. We initialize pairs of atoms in the $|1\rangle \equiv |m_F = +1/2\rangle$ sublevel of the $6s6p\,^3P_0$ metastable state. Static magnetic fields are applied at 90° ($\theta = \pi/2$) with respect to the internuclear separation. Transitions into Rydberg-pair states are subsequently driven by a two-photon transition detuned by $\Delta E$ from the asymptotic case of two isolated Rydberg atoms. Pairs of atoms transferred to Rydberg states are blown out of the optical tweezers by driving a transition (369 nm) into an autoionizing state [99]. Remaining atoms in the $|1\rangle$ state are depumped into the $^1S_0$ ground state for fluorescence imaging. The excitation of a Rydberg-pair state is inferred by conditioning the remaining atom population after a given experimental sequence on pairwise atom loss. An exemplary pair-state spectrum close to the $|54.28, L = 0, F = 1/2, -1/2\rangle^{\otimes 2}$ asymptotic pair state is given in Fig. 10(c). For a given optical tweezer separation, we observe an increase in pairwise atom loss when tuning the two-photon transition over a Rydberg-pair state. The pair-state resonance shifts to larger two-photon detuning when reducing the tweezer separation, indicating a larger interaction between the two Rydberg atoms. We fit the observed pair-state spectra using a Gaussian line-shape model. The resulting center frequency of the fits are presented in Figs. 6 and 7.

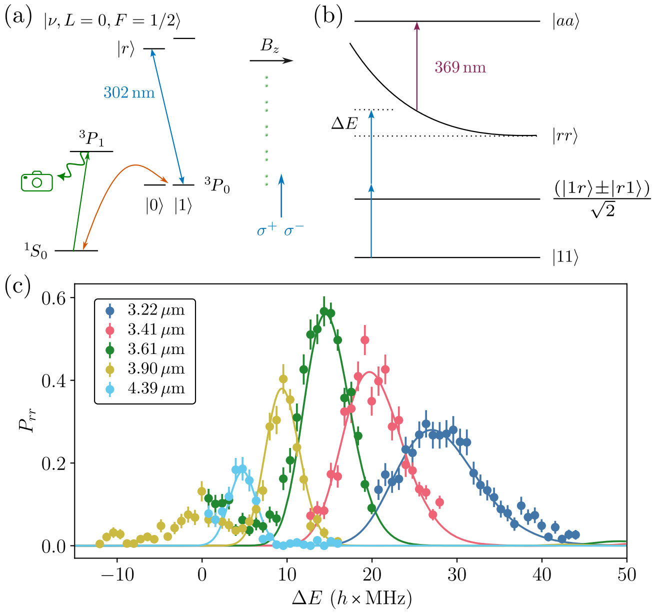

FIG. 10. (a) Single-atom transition scheme for measuring interactions between pairs of Rydberg atoms in an optical tweezer setup [40]. The $^{171}$Yb atoms are prepared states in the $|1\rangle$ sublevel of the $^3P_0$ metastable state. Transitions to the $|\nu, L = 0, F\rangle$ Rydberg state are driven by a single-photon transition (302 nm). For rearrangement and readout, the atoms are imaged by collecting the fluorescence on the $|^1S_0\rangle \leftrightarrow |^3P_1\rangle$ transition. (b) Scheme for measuring Rydberg-Rydberg interactions between pairs of single atoms trapped in optical tweezer arrays. (c) Experimental pair-state spectra (solid dots) obtained by recording the probability of pairwise loss from tweezers in fluorescence image as a function of the two-photon detuning and tweezer separation. The error bars represent the standard deviation of the measured values observed across repeated iterations of the experiment. The experimental spectra are compared to simulated pair spectra $S(E)$ (solid lines) obtained from Eq. (C1), as explained in the text.

On top of the shift of the pair-state resonance, we also observe a broadening. We attribute the observed broadening to the spatial fluctuations of the single atoms in the optical tweezers ($T \approx 3$ μK). Because of the spatial fluctuations of the atoms, the linewidth of the pair-state resonance is affected by the gradient of the interaction potential, which increases toward shorter internuclear separations. To model the effect of fluctuating internuclear separations in the optical tweezers, we simulate the pair-state spectra $S(E)$,

$$S(E) \propto \sum_{\Phi} \mathcal{G}(E - E_\Phi(R), \sigma_E)\, \mathcal{T}(R - \tilde{R}, \sigma_R)\, \mathcal{O}_{\Phi,\Phi'}(R), \tag{C1}$$

where the sum runs over all relevant pair state $\Phi$ coupled to the target state $\Phi'$, $E_\Phi(R)$ is the internuclear-separation-dependent pair-state energy, $\tilde{R}$ is the mean internuclear separation, $\mathcal{G}(E - E_\Phi(R), \sigma_E)$ is a function describing the experimental linewidth of the spectrum in the absence of any broadening, $\mathcal{T}(R - \tilde{R}, \sigma_R)$ is a function describing the distribution of internuclear separation around a mean separation $\tilde{R}$, and $\mathcal{O}_{\Phi,\Phi'}(R)$ is the overlap coefficient.

For the case presented in Fig. 10(c), the line broadening can be reproduced by assuming a normal distribution in the internuclear separations with standard deviation of 100 nm. This is close to the expected distance fluctuations of approximately 50 nm between two atoms confined in optical tweezers with radial and axial trap frequencies of $\omega_r = 60$ kHz and $\omega_z = 10$ kHz, respectively.

## APPENDIX D: ADDITIONAL SPECTROSCOPIC DATA AND MODELS FOR $^{174}$Yb

In this appendix, we give additional details of the spectroscopic measurements and MQDT model development for $^{174}$Yb. We also make comparisons between the MQDT model and previously measured quantities, including singlet-triplet mixing in the $^{1,3}P_1$ and $^{1,3}D_2$ series, and diamagnetic shifts in the P series.

### 1. $^3S_1$ and $^1S_0$

For the $n\,^1S_0$ Rydberg series of $^{174}$Yb, we adapt the six-channel MQDT model presented in previous work [49]. We refit the MQDT model parameters of the $^1S_0$, $^{1,3}D_2$, $^{1,3}P_1$ Rydberg series in a simultaneous, 42-parameter fit to the previously measured [46,49,50,53–56,58] and newly measured data presented in Supplemental Material [70], leveraging the higher-precision microwave measurements between $S$, $D$, and $P$ Rydberg states. The resulting MQDT models are presented in Supplemental Material Tables S1–S3 [70].

For the $n\,^3S_1$ with $n > 28$, we adapt the single-channel quantum defect model with a Rydberg-Ritz expansion for the energy-dependent quantum defect presented in Ref. [29].

### 2. $^1P_1$ and $^3P_1$

Here we introduce a six-channel MQDT model for the $^{1,3}P_1$ Rydberg series of $^{174}$Yb. Compared to the five-channel model presented in Ref. [50], we introduce a sixth perturbing channel, which lies energetically above the first ionization limit of $^{174}$Yb. The addition of the sixth channel was necessary to accurately describe the energies of the high-$n$ states of this series. In addition, we introduce singlet-triplet mixing between the $^1P_1$ and $^3P_1$ explicitly, by introducing a rotation to the $U_{i\alpha}$ matrix, $\theta_{12}$ whose value is constrained by the Stark shift of the $^1S_0$ state, as explained in Sec. II.

We extend the previously measured state energies of $^{1,3}P_1$ [50,56] by measuring microwave transition frequencies between $n\,^{1,3}P_1$ and $n'\,^{1,3}D_2$ or $n'\,^1S_0$ Rydberg states in the range of $31 \leq n \leq 43$, as summarized in Supplemental Material Tables S18 and S19 [70]. We cross-checked several transition frequencies reported in Ref. [50] and generally found good agreement within the stated error bars, with the exception of the $6s45p\,^3P_1 \leftarrow 6s44s\,^1S_0$, which deviated from our new measurement and the final theoretical prediction from the MQDT model by nearly 10 MHz. We therefore do not include this data point in our analysis. In the fitting procedure, we optimize the 42 parameters of the $^1S_0$, $^{1,3}D_2$, $^{1,3}P_1$ MQDT models in a simultaneous fit to the data presented in Supplemental Material [70]. The resulting MQDT models are presented in Supplemental Material Tables S1–S3 [70].

The presented MQDT model correctly predicts the energies of the highly excited $n\,^{1,3}P_1$ Rydberg states (Fig. 11). However, below $\nu < 15$, significant deviations between the experimental and theoretical energies occur. This could be due to unaccounted perturbing channels, either directly in the low-$\nu$ regime, or in the high-$\nu$ regime, with the current MQDT model parameters overcompensating trends in the quantum defects for the more accurately determined Rydberg states at high $\nu$.

The breakdown of pure $LS$ coupling in the $^{1,3}P_1$ Rydberg channels is quantified by measuring the static dipole polarizabilities of $n\,^1S_0$ Rydberg states in the vicinity of a near degeneracy with dominantly $n\,^3P_1$ Rydberg states, as discussed in the main text. To obtain the best agreement between the experimental and theoretical static polarizabilities of the $n\,^1S_0$ Rydberg states, an energy-dependent singlet-triplet mixing angle [refer to Eq. (A10)] had to be introduced. The resulting MQDT parameters are presented in Supplemental Material [70].

With the obtained $J = 1$ (odd parity) MQDT model for $^{174}$Yb and using Eq. (A18), we can estimate the $6snp\,^3P_1$ channel contribution into the nominally $n\,^1P_1$ Rydberg states. The resulting values are presented in Fig. 12 and compared to values obtained from previous measurements of diamagnetic shifts, as presented in Ref. [57] and from previous hyperfine-structure measurements in $^{171}$Yb and $^{173}$Yb, as presented in Ref. [71]. The theoretically obtained values for the triplet contribution to the $n\,^1P_1$ Rydberg states agree well with the previously reported values between $20 \leq n \leq 100$, but with significantly reduced uncertainties, highlighting the sensitivity of measuring matrix elements through Stark shifts close to near degeneracies.

As an additional check of the validity of the model, we compare the predicted Zeeman and diamagnetic shifts in very large magnetic fields to a previous experimental measurement from Ref. [57]. In that work, the measured energies were fit with a phenomenological model to extract the singlet-triplet splitting for that $n$. In Fig. 13, we show the prediction of the MQDT model with no free parameters, finding excellent agreement.

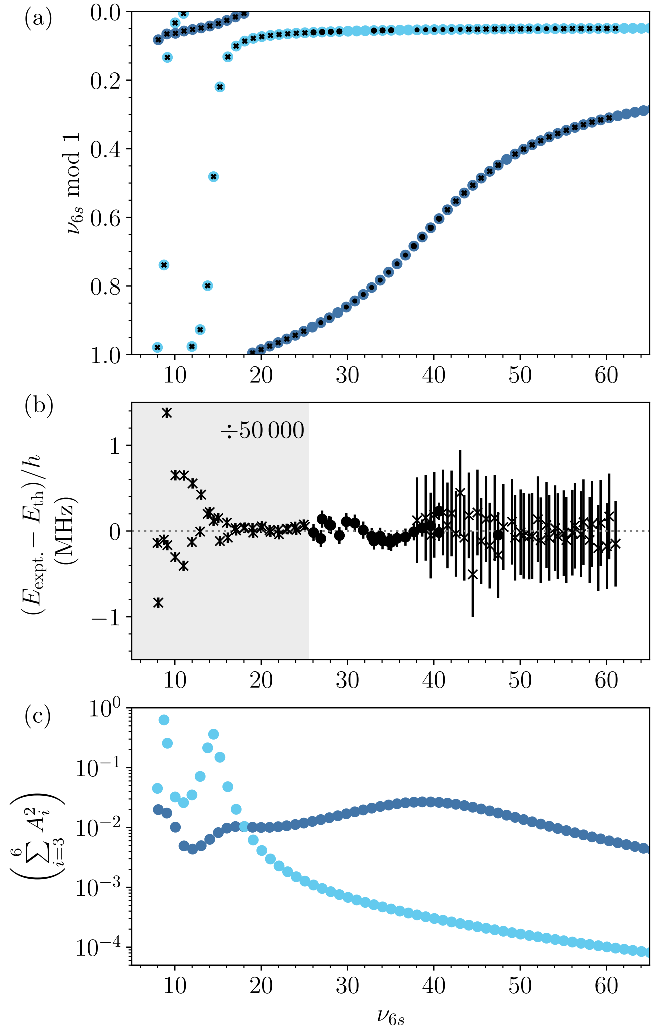

FIG. 11. (a) Lu-Fano-type plot of the $^{174}$Yb $^{1,3}P_1$ Rydberg series. The theoretical bound states with dominant singlet and triplet character are indicated by light and dark blue dots, respectively. Experimentally observed states are indicated by black crosses (Refs. [50,56]) and black dots (this work). The error bars correspond to the respective measurement uncertainties. (b) Deviation between experimental and theoretical state energies. The energy deviations and error bars in the gray shaded area are scaled by a factor of 50 000 to improve visibility of the much smaller errors observed on the microwave transitions. (c) Perturbing channel fraction $\sum_{i=3}^{6} A_i^2$ of the dominantly singlet (light blue) and triplet (dark blue) Rydberg states.

### 3. $^3P_2$

Here, we introduce a four-channel MQDT model for $^3P_2$ Rydberg states of $^{174}$Yb. In comparison to the previously presented three-channel MQDT model from Ref. [48], we introduce an additional channel with a perturbing state above the first ionization limit. The addition of the fourth channel was necessary to accurately describe the energies of the high-$n$ states of this series.

The MQDT model parameters are optimized in a weighted least-squares procedure. The Rydberg state

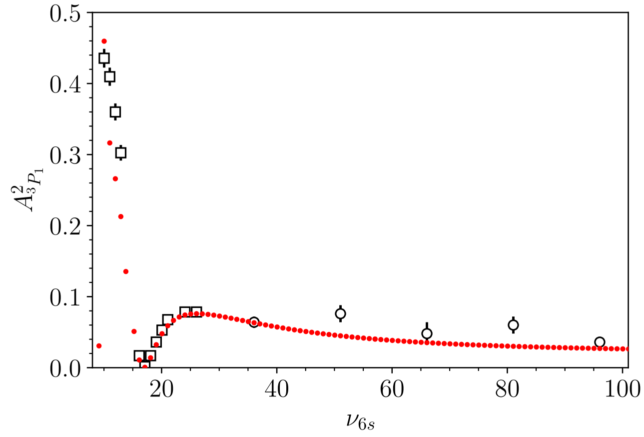

FIG. 12. $6snp\,^3P_1$ character ($A^2_{^3P_1}$) in $6snp\,^1P_1$ Rydberg states of $^{174}$Yb. The open black squares correspond to experimental values obtained by measurements of the hyperfine structure of $^{171}$Yb and $^{173}$Yb $^{1,3}P_1$ Rydberg states from Ref. [71]. The open black circles correspond to experimental values obtained by measuring diamagnetic shifts taken from Ref. [57]. The error bars are directly taken from Refs. [57,71]. The full red circles correspond to theoretical values of $A^2_{^3P_1}$ as obtained from the MQDT model presented in Supplemental Material Table S3 [70].

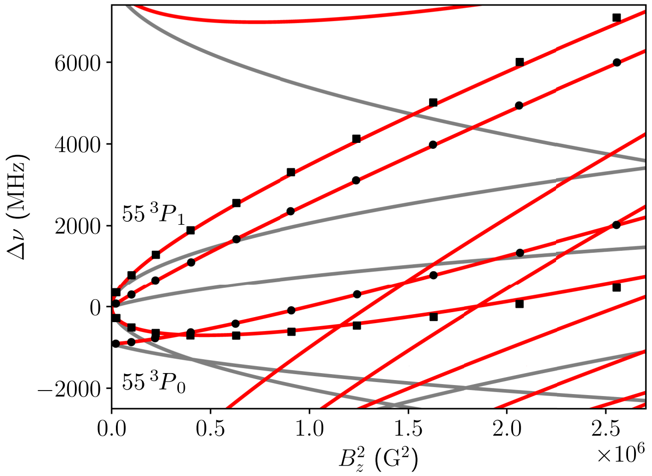

FIG. 13. Zeeman shifts of $^{174}$Yb Rydberg states near the 55 $^3P_1$ state. The red and gray curves correspond to Zeeman shift calculations with and without diamagnetism, respectively. The near degeneracy of the 55 $^3P_0$ and 55 $^3P_1$ states leads to a strong interaction between the 55 $^3P_1(m_J = 0)$ and 55 $^3P_0(m_J = 0)$ sublevels. The black circles and squares correspond to experimentally observed Zeeman shifts extracted from Fig. 3 of Ref. [57] for the $m_J = 0$ and $m_J = \pm 1$ sublevels, respectively. The experimental Zeeman shifts from Fig. 3 of Ref. [57] are plotted directly for the $m_J = 0$ states, whereas the values for the $m_J \pm 1$ states are obtained from the mean experimental diamagnetic shifts and theoretical predictions for the paramagnetic contribution to the Zeeman shift.

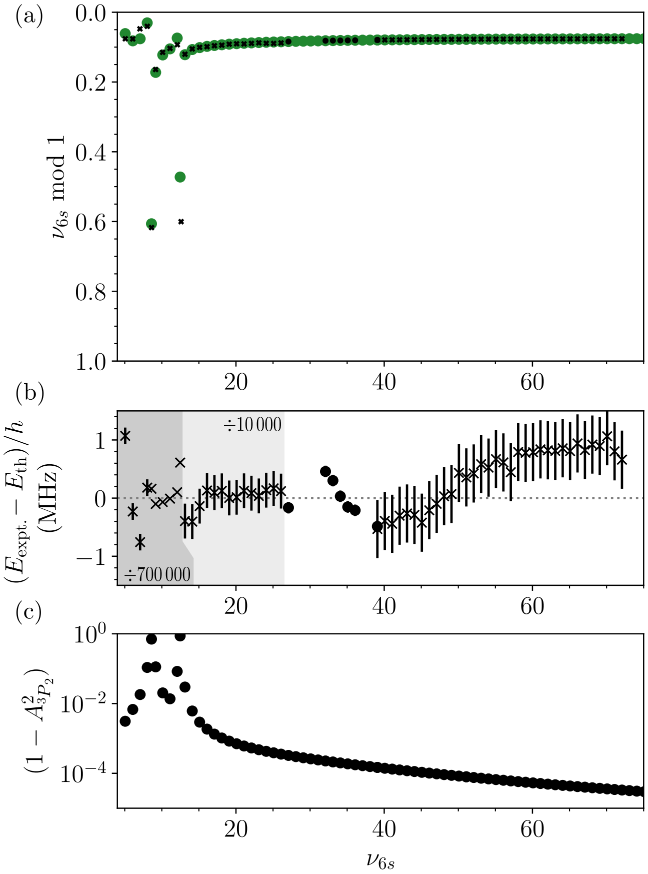

FIG. 14. (a) Lu-Fano-type plot of the $^{174}$Yb $^3P_2$ Rydberg series. The theoretical bound states are indicated by green dots. Experimentally observed states are indicated by black dots (Refs. [50,56]) and dots (this work). The error bars correspond to the respective measurement uncertainties. (b) Deviation between experimental and theoretical state energies. The energy deviations and error bars in the light (dark) gray shaded area are scaled by a factor of 10 000 (700 000) to improve visibility of the much smaller errors observed on the microwave transitions. (c) Perturber fraction $(1 - A^2_{^3P_2})$ of the Rydberg states in the $(J = 2)^o$ Rydberg series.

energies includes in the fitting procedure include previously measured state energies of $^3P_2$ by laser [56] and microwave spectroscopy [50], as well as newly measured microwave transition frequencies between $n\,^3P_2$ and $n'\,^3D_2$ Rydberg states in the range of $31 \leq n \leq 43$. The included Rydberg state energies and the resulting MQDT model parameters are presented in Supplemental Material [70].

As depicted in Figs. 14(a) and 14(b), the newly introduced MQDT model for $^3P_2$ captures the energies of the highly excited $n\,^3P_2$ Rydberg state quantitatively, but qualitatively captures only the energies of the states in the strongly perturbed range below $\nu \approx 15$.

Figure 14(c) depicts the contribution of the core-excited channels, which are below $10^{-3}$ for states with $\nu > 20$, confirming a mostly unperturbed $^3P_2$ Rydberg series. Series perturbers can shorten the lifetime of Rydberg states even at high $n$ by introducing an additional decay channel proportional to $\sum A_i \Gamma_i$, where $\Gamma_i$ is the decay rate of the perturbing states. Since $\Gamma_i$ for low-lying atomic states can be substantially faster than for Rydberg states, even a small admixture can significantly alter the lifetime. We note that Ref. [29] measured the lifetime of the 74 $^3P_2$ state to be 83(5) μs, which is close to but slightly shorter than the lifetime predicted for a $P$ state of $^{87}$Rb with a similar quantum number (approximately 200 μs at $T = 300$ K [123]). This is qualitatively consistent with the modeled small but nonzero perturbation of this series. A quantitative assessment will require predictions for matrix elements and decay rates of the perturbing states, which is a subject for future work.

### 4. $^3P_0$

Here, we present a two-channel MQDT model for the $n\,^3P_0$ Rydberg states of $^{174}$Yb. A two-channel model suffices to reproduce the observed states at high $n$, though we believe additional channels will eventually be necessary to explain the full series. We have no direct information about the nature of the perturbing series and follow Ref. [56] by assigning a perturbing channel with character $4f^{13}5d6snd\,^3P_0$ (labeled $Q$). The MQDT model parameters are optimized in a weighted least-squares fit to both previously measured state energies by laser spectroscopy [56] and newly measured state energies from microwave spectroscopy summarized in Supplemental Material Tables S24 and S23 [70], respectively.

The $n\,^3P_0$ Rydberg states are inaccessible by direct one-photon microwave transitions from laser-accessible $n\,^1S_0$ and $n\,^{1,3}D_2$ Rydberg states. Instead, we perform spectroscopy on $n\,^3P_0$ Rydberg states of $^{174}$Yb by utilizing the Autler-Townes splitting on a probe transition. To this extent, we monitor the resonant population transfer on the two-photon $n\,^3D_2 \to n'\,^3S_1$ microwave transition as a function of the frequency of a simultaneously applied microwave pulse coupling the $n\,^3S_1 \to n''\,^3P_0$ transition. The observed $n\,^3P_0 \leftrightarrow n'\,^3D_2$ intervals are summarized in Supplemental Material Table S23 [70]. We recorded a total of six transitions to $n\,^3P_0$ Rydberg states in the range of $31 \leq n \leq 49$, which were particularly necessary to determine the energy dependence of the strongly perturbed $^3P_0$ series. The results of this measurement, together with previous three-photon laser spectroscopy [56], are presented in Supplemental Material [70].

The obtained MQDT model is summarized in Supplemental Material Table S5 [70] and presented in a Lu-Fano-like plot in Fig. 15. The MQDT model represents the experimental data well within the experimental uncertainties over a range of $18 \leq n \leq 50$.

The contributions of perturbing channel $Q$ into the $n\,^3P_0$ Rydberg states is presented in Fig. 15(c). The channel

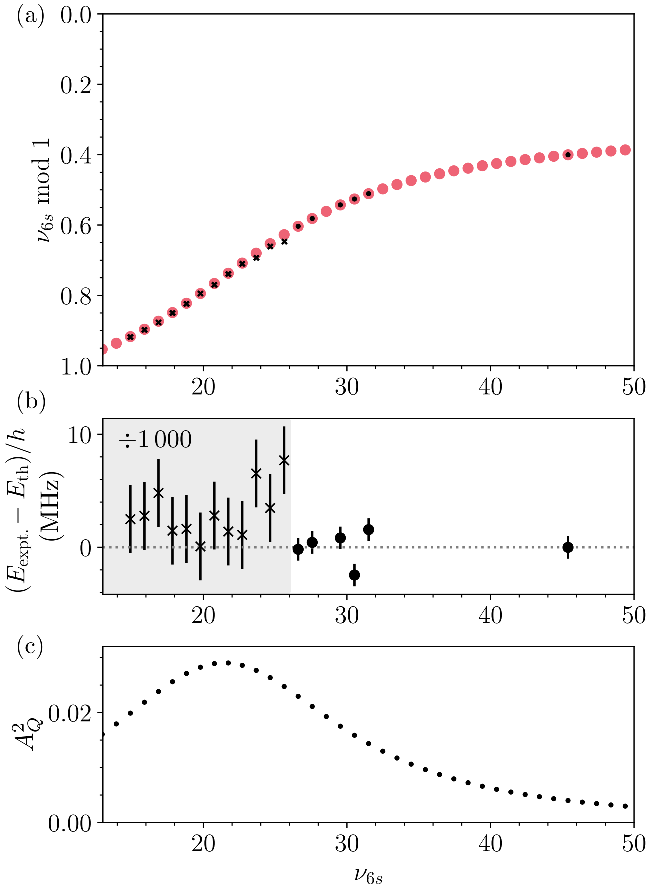

FIG. 15. (a) Lu-Fano-type plot of the $^{174}$Yb $^3P_0$ Rydberg series. The theoretical bound states are indicated by red dots. Experimentally observed states are indicated by black crosses (Ref. [56]) and dots (this work). The error bars correspond to the respective measurement uncertainties. (b) Deviation between experimental and theoretical state energies. The energy deviations and error bars in the gray shaded area are scaled by a factor of 1000 to improve visibility of the much smaller errors observed on the microwave transitions. (c) $Q$-channel contribution $A_Q^2$ to the $n\,^3P_0$ Rydberg states.

contribution is spread out over a wide range of principal quantum numbers and reaches a maximum value of approximately 3% at $n = 26$. This is consistent with a significantly reduced lifetime of the 74 $^3P_0$ Rydberg state [14(4) μs] observed in Ref. [29]. Further refinement of the MQDT model for this series at low $n$ will be useful to understand the lifetimes of this series quantitatively.

### 5. $^1D_2$ and $^3D_2$

Here, we present a five-channel MQDT model for the $n\,^{1,3}D_2$ Rydberg states of $^{174}$Yb. We adapt this model from Ref. [49], but we refit the MQDT model parameters of the $^1S_0$, $^{1,3}D_2$, $^{1,3}P_1$ Rydberg series in a simultaneous, 42-parameter fit to the previously measured [46,49,50,53–56,58] and newly measured data presented in Supplemental Material [70]. The resulting MQDT models are presented in Supplemental Material Tables S1–S3 [70].

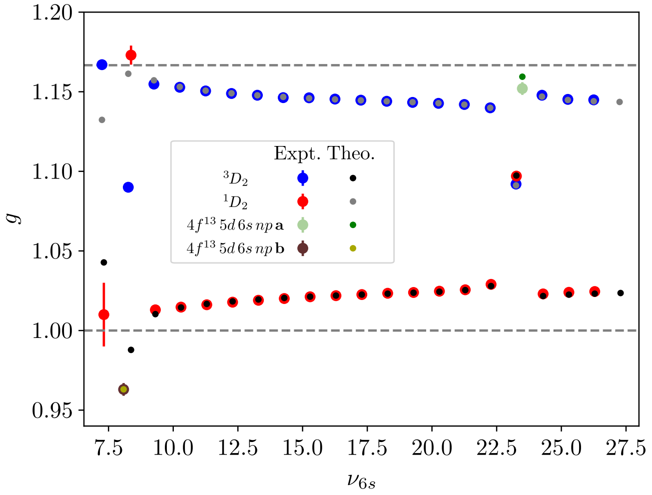

FIG. 16. $g$ factors of the $^{1,3}D_2$ and its perturbers as taken from Ref. [59] and calculated with the MQDT presented in Supplemental Material Table S2 [70]. The error bars of the experimental data are taken directly from Ref. [59] indicating the combined uncertainties from statistical variations, magnetic field calibration, and residual systematic errors. The gray dashed lines indicate the values for $g$ factors in pure $LS$ coupling.

In addition, to account for singlet-triplet mixing, the model includes a rotation around the $^1D_2$ and $^3D_2$ channels in the $U_{i\alpha}$ matrix. To determine the magnitude of the singlet-triplet mixing, we use the $g$ factors of the $n\,^{1,3}D_2$ Rydberg series and its perturbers measured by Zerne *et al.* [59] to obtain a value for the singlet-triplet mixing angle between the $^1D_2$ and $^3D_2$ channels. To that extent, we vary the energy-dependent mixing angle $\theta_{12}$ [Eq. (A10)] and calculate the $g$ factor in using Eq. (22) of Ref. [44]. In addition, we treat the $g$ factors of the perturbing states with only partially known electronic configuration as parameters of our model. To obtain the best agreement between experiment and theory, we introduce an energy-dependent mixing angle, as defined in Eq. (A10). The results of the fit are presented in Fig. 16, and the MQDT model is summarized in Supplemental Material Table S2 [70]. From our MQDT model, we estimate a triplet character in the $^1D_2$ series between 14.0% and 15.5% for $30 \leq n \leq 100$. This is in agreement with an estimated triplet admixture into the $36\,^1D_2$ state of 19(6)% presented in Ref. [58].

### 6. $^3D_1$ and $^3D_3$

The $^3D_1$ and $^3D_3$ Rydberg states of $^{174}$Yb are not directly laser accessible by two-photon laser spectroscopy through the $6s6p$ $^1P_1$ intermediate state. A few $^3D_1$ and $^3D_3$ Rydberg states have been observed in Refs. [61,124]. For the purposes of this work, we infer the quantum defects of the $^3D_1$ and $^3D_3$ from laser-accessible $D$

TABLE I. Rydberg-Ritz expansion coefficients of the $n\ ^3D_1$ and $n\ ^3D_3$ Rydberg states of Yb inferred from laser spectroscopy of $D$ $F = 3/2$ and $F = 5/2$ Rydberg states of $^{171}$Yb.

| | $n\ ^3D_1$ | $n\ ^3D_3$ |
|---|---|---|
| $\mu_0$ | 2.752 580 93 | 2.728 953 15 |
| $\mu_2$ | 0.3826 | −0.2065 |
| $\mu_4$ | −483.1 | 220.5 |

$F = 3/2$ and $D$ $F = 5/2$ Rydberg states in $^{171}$Yb, as discussed in Appendix E 3.

The quantum defects of the two series are well described by a Rydberg-Ritz model

$$\mu(n) = \mu_0 + \frac{\mu_2}{(n-\mu_0)^2} + \frac{\mu_4}{(n-\mu_0)^4} \qquad \text{(D1)}$$

for the states studied in this work with $\nu > 30$. The obtained expansion coefficients for the two series are presented in Table I.

The inferred quantum defects for the $n\ ^3D_3$ Rydberg series are consistent with the assignment of measurements in $^{174}$Yb presented in Ref. [61] to within the stated measurement uncertainties of 10 MHz. The inferred quantum defects for the $n\ ^3D_1$ Rydberg series are consistent with the assignment of measurements in $^{174}$Yb presented in Refs. [61,124], but the Rydberg state energies deviate up to 40 MHz from the values presented in Ref. [61], which could be due to the limited number of $D$ $F = 3/2$ states with dominant $^3D_1$ character observed in this work.

## APPENDIX E: ADDITIONAL SPECTROSCOPIC DATA AND MODELS FOR $^{171}$Yb

In this appendix, we give additional details about the spectroscopic measurements and MQDT model development for $^{171}$Yb.

### 1. $S$ $F = 1/2$ and $F = 3/2$ states

There is only a single $F = 3/2$ series with $L = 0$, which converges to the $F_c = 1$ threshold and has $^3S_1$ character. We have measured the energy spacing between several $S$ $F = 3/2$ Rydberg states and $S$ $F = 1/2$ or $D$ $F = 5/2$ Rydberg states using microwave spectroscopy in an atomic beam. The experimental transition frequencies are presented in Supplemental Material Table S29 [70]. Because of the small number of measured transitions to $S$ $F = 3/2$ Rydberg states, we model this series using the Rydberg-Ritz model introduced for $^{174}$Yb [29] with parameters optimized in the fit to the $S$ $F = 1/2$ Rydberg states (presented in Supplemental Material Table S6 [70]). The experimental and theoretical energies of the $S$ $F = 3/2$ Rydberg series agree to within the uncertainty of the initial state energy used in the microwave spectroscopy.

In Fig. 5, we presented measurements of Stark shifts of $S$ $F = 1/2$ Rydberg states. Most Rydberg states exhibit a quadratic Stark shift at small electric fields, common for nondegenerate Rydberg states, and we extract a static polarizability by a quadratic fit to the observed Stark shift. However, for cases in which the Rydberg state of interest is very nearly degenerate with other Rydberg states (shaded gray in Fig. 5), the Stark shift is not quadratic even at very small electric fields. In Fig. 17, we present a field-dependent shift measurement together with a nonperturbative calculation, finding excellent agreement, highlighting the accuracy of the obtained Rydberg state energies and wave functions obtained by our MQDT treatment.

Figure 18 illustrates calculated transition dipole matrix elements from the $6s6p\ ^3P_0$ metastable state into $S$ ($F = \{1/2, 3/2\}$) Rydberg states of $^{171}$Yb, which are computed using the single active electron approximation. The matrix elements to $S$ ($F = 1/2$) Rydberg states are generally smaller than the matrix elements to $S$ ($F = 3/2$) Rydberg states. However, at low effective principal quantum numbers, the transition dipole matrix element to one of the two $S$ ($F = 1/2$) Rydberg series is still comparable to the $S$ ($F = 3/2$) case, due to a dominant triplet character. At larger effective principal quantum numbers, particularly close to near degeneracies between the two $S$ ($F = 1/2$) channels, the matrix elements vary strongly with the effective principal quantum number, indicating strong hyperfine-induced singlet-triplet mixing.

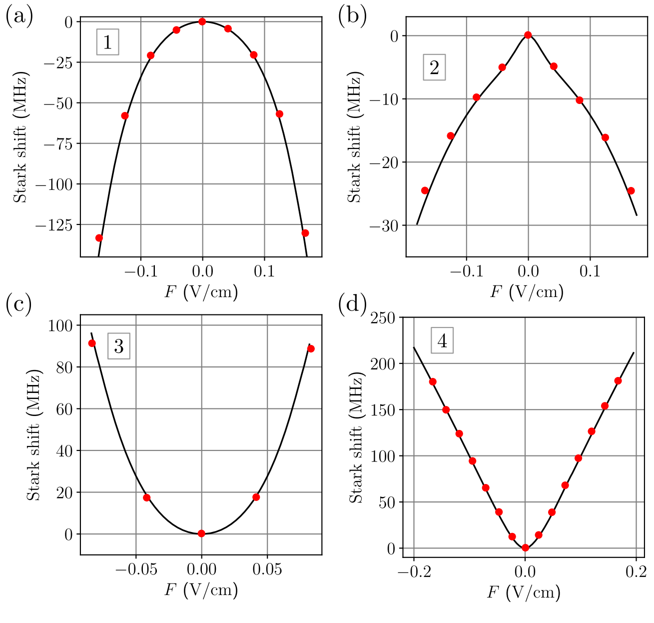

FIG. 17. Experimental Stark shifts (red dots) of $^{171}$Yb $|\nu_{F_c=1}, L = 0, F = 1/2\rangle$ Rydberg states with (a) $\nu_{F_c=1} \approx 65.68$, (b) $\nu_{F_c=1} \approx 66.68$, (c) $\nu_{F_c=1} \approx 67.68$, (d) $\nu_{F_c=1} \approx 64.09$ compared with theoretical Stark shifts (solid black line). The extracted experimental Stark shifts at low electric field are presented in subpanels of Figs. 5(d) and 5(e) as indicated by labels 1 to 4.

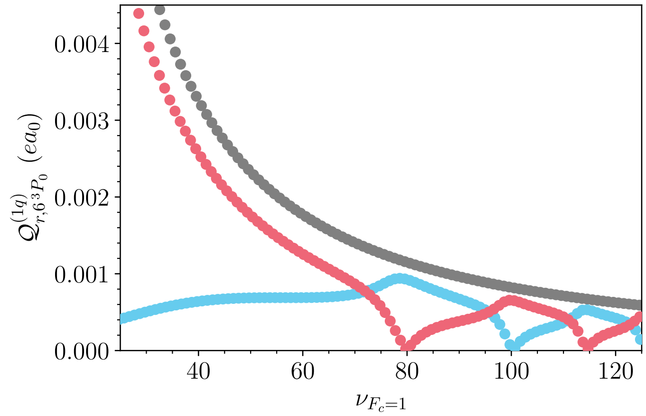

FIG. 18. Transition dipole matrix elements $\mathcal{Q}_{r,6^3P_0}$ between the $6s6p\ ^3P_0(m_F = +1/2)$ metastable and Rydberg state $r$, where $r = |\nu, L = 0, F = 3/2, m_F = +3/2\rangle$ (gray) and $r = |\nu, L = 0, F = 1/2, m_F = -1/2\rangle$ (red and blue, color code as in Fig. 3).

### 2. *P* $F = 1/2$, $F = 3/2$, and $F = 5/2$ states

Here, we introduce MQDT models for $P$ $F = 1/2$, $F = 3/2$, and $F = 5/2$ Rydberg states of $^{171}$Yb. There are seven $L = 1$ series in $^{171}$Yb. In *LS* coupling, they can be described as $^3P_0(F = 1/2)$, $^1P_1(F = \{1/2, 3/2\})$, $^3P_1(F = \{1/2, 3/2\})$, and $^3P_2(F = \{3/2, 5/2\})$. As in the case of the $|\nu, L = 0, F = 1/2\rangle$, we use the $^{174}$Yb MQDT models of $^{1,3}P_1$ and $^3P_0$ (for $F = 1/2$) and $^{1,3}P_1$ and $^3P_2$ (for $F = 3/2$) as a basis for the $^{171}$Yb MQDT model and introduce the hyperfine coupling in the ion-core using a frame transformation (see Appendix A 2).

We optimize the MQDT model parameters for both the $F = 1/2$ and $F = 3/2$ series using a weighted, least-squares fitting procedure to a dataset containing Rydberg state energies obtained in this work from microwave spectroscopy (Supplemental Material Tables S30 and S33 [70]) and from previous laser spectroscopy reported Ref. [71] (Supplemental Material Tables S31 and S34 [70]). In our fitting procedure, we treat all $^{171}$Yb MQDT model parameters originating from the same $^{174}$Yb MQDT models as a single parameter. For example, both the $^{171}$Yb $P$ $F = 1/2$ and $P$ $F = 3/2$ MQDT models contain a contribution from the $^{1,3}P_1$ MQDT model developed for $^{174}$Yb in Appendix D 2. The resulting MQDT parameters for $F = 1/2$ and $F = 3/2$ are presented in Supplemental Material [70].

The state energies reported in Supplemental Material Tables S31 and S34 [70] are obtained from isotope shift and hyperfine-splitting measurements of the $n\,^1P_1$ and $n\,^3P_{0,1,2}$ Rydberg states using three-photon laser spectroscopy, as presented in previous work [71] (reproduced in Supplemental Material Tables S36 and S37 [70]). The isotope shift and hyperfine splittings in Ref. [71] are given with respect to $6snp\,^1P_1$ and $6snp\,^3P_1$ Rydberg states of $^{176}$Yb (reproduced in Supplemental Material Table S38 [70]). The absolute uncertainty of the $^{176}$Yb Rydberg state energies presented in Ref. [71] is stated to be 4 GHz, but we find that the stated (relative) hyperfine splittings are more precise. To remove systematic errors on the inferred absolute energies of the $^{171}$Yb $P$ $F = 1/2$ and $F = 3/2$ Rydberg states, we introduce the following treatment.

For Rydberg states with principal quantum number $n > 20$, Ref. [71] reports a nearly constant isotope shift between $^{1,3}P_1$ Rydberg states of $^{174}$Yb and $^{176}$Yb. For $n > 20$, we therefore choose to reference the hyperfine splittings against the accurate energies obtained from the $^{174}$Yb $^{1,3}P_1$ MQDT model presented in Appendix D 2. The remaining isotope shift between $^{171}$Yb and $^{174}$Yb Rydberg states is accounted for by introducing a constant shift to inferred absolute energies in order to minimize the deviations to absolute energies inferred from microwave intervals to the $|\nu, L = 0, F = 1/2\rangle$ Rydberg states.

For low-lying states $^{1,3}P_1$ of $^{174}$Yb, we observe significant deviations between experimental and predicted energies for $^{174}$Yb (Appendix D 2). For $n \leq 20$, we therefore choose to infer absolute energies of the observed $P$ Rydberg states in $^{171}$Yb by referencing the hyperfine-splitting measurements to the observed absolute energies of $^{176}$Yb, as presented in Ref. [71] (reproduced in Supplemental Material Table S38 [70]). When applying this treatment to the Rydberg state with $n > 20$, we observe a systematic shift of the inferred energies compared to the more accurate absolute state energies obtained from microwave intervals to the $|\nu, L = 0, F = 1/2\rangle$ Rydberg states. The mean deviation is approximately 1.4 GHz and is well within the 4-GHz uncertainty stated for the $^{176}$Yb term values reported in Ref. [71]. In an attempt to remove this systematic shift, we add a constant energy offset to all $^{171}$Yb $P$ Rydberg states that were referenced to the $^{176}$Yb energies.

The resulting inferred absolute energies of $|\nu, L = 1, F = 1/2\rangle$ and $|\nu, L = 1, F = 3/2\rangle$ Rydberg states are presented in Supplemental Material Tables S31 and S34 [70].

### 3. *D* $F = 1/2$, $F = 3/2$, $F = 5/2$, and $F = 7/2$

There are eight $L = 2$ series in $^{171}$Yb. In *LS* coupling, they can be described as $^3D_1(F = \{1/2, 3/2\})$, $^1D_2(F = \{3/2, 5/2\})$, $^3D_2(F = \{3/2, 5/2\})$, and $^3D_3(F = \{5/2, 7/2\})$. In $^{174}$Yb, spin-orbit coupling mixes the two $J = 2$ series as discussed in Sec. II; in $^{171}$Yb, hyperfine coupling additionally mixes the three $F = 3/2$ series and the three $F = 5/2$ series.

As in the case of the $|\nu, L = 0, F = 1/2\rangle$ Rydberg states, we measure the energies of $|\nu, L = 2, F = 3/2\rangle$ and $|\nu, L = 2, F = 5/2\rangle$ Rydberg states by laser spectroscopy by a two-photon transition via the $6s6p\,^1P_1(F = 3/2)$ intermediate state. Transition frequencies to all measured $|\nu, L = 2, F = 3/2\rangle$ and $|\nu, L = 2, F = 5/2\rangle$ states are

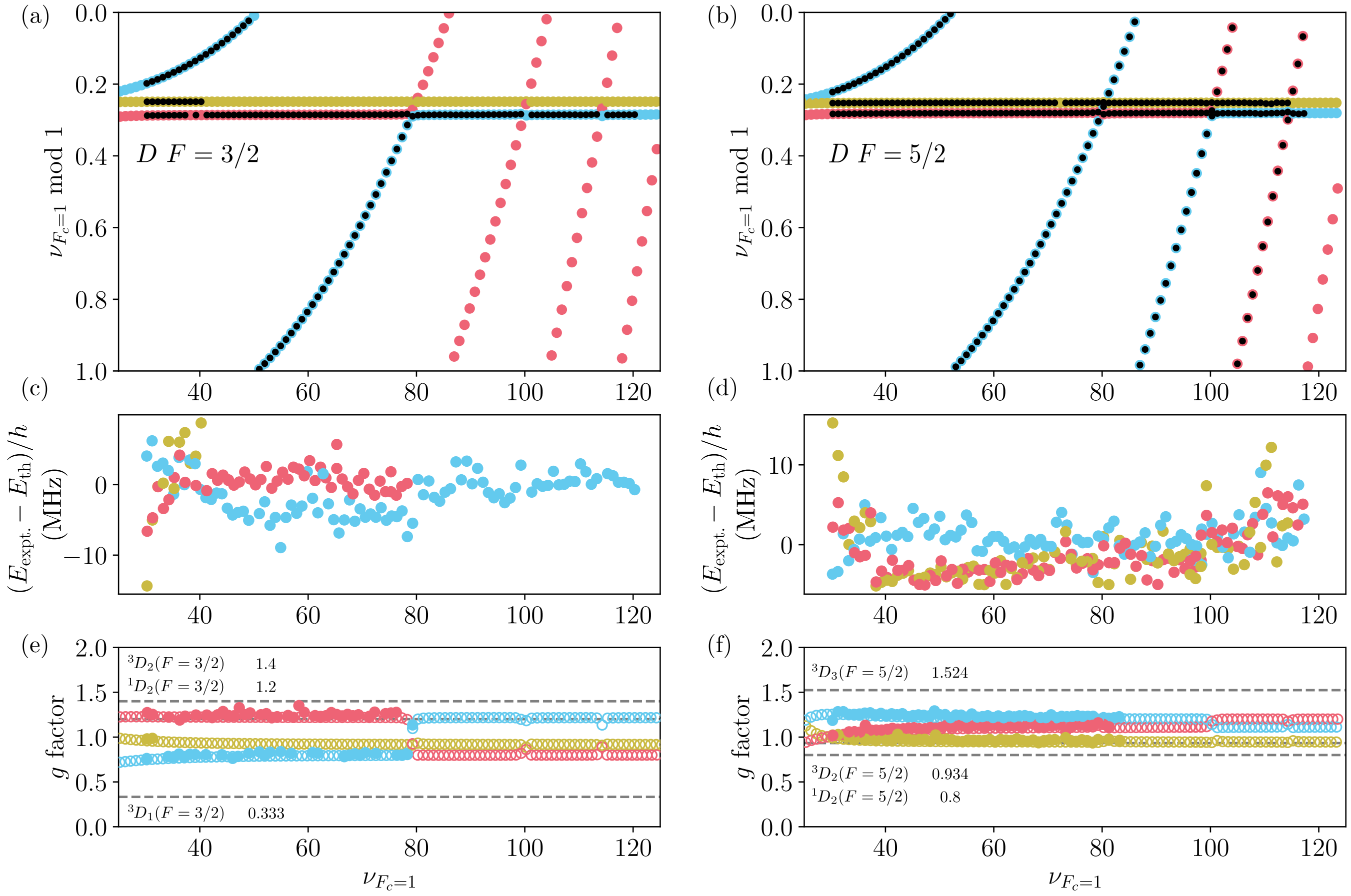

FIG. 19. Lu-Fano-type plot of the $^{171}$Yb (a) $|\nu, L = 2, F = 3/2\rangle$ and (b) $|\nu, L = 2, F = 5/2\rangle$ Rydberg states. The experimentally observed Rydberg states are indicated by black dots and compared to theoretically obtained energies from the MQDT model (colored dots) presented in Supplemental Material Tables S9 and S10 [70]. (c),(d) Deviations between the experimentally observed and theoretically calculated state energies. (e),(f) Experimentally observed (full circles) and theoretically calculated $g$ factors of the $|\nu, L = 2, F = 3/2\rangle$ and $|\nu, L = 2, F = 5/2\rangle$ Rydberg states, respectively. Color coding as in (a) and (b). The gray dashed lines indicate the values of Landé $g$ factors in pure $LS$ coupling.

summarized in Supplemental Material [70] and plotted on a Lu-Fano-type plot in Fig. 19(a).

We use a least-squares procedure to obtain the MQDT parameters for the $F = 3/2$ and $F = 5/2$ series. As in the case of the $P$ Rydberg states, we treat the MQDT parameters that originate from the $^{174}$Yb models and occur in both the $F = 3/2$ and $F = 5/2$ MQDT models as a single parameter. The developed MQDT models describe both the Rydberg state energies and the measured $g$ factors (summarized in Supplemental Material [70]) well over nearly the entire energy range. Significant deviations for both $F = 3/2$ and $F = 5/2$ occur toward low effective principal quantum numbers. These deviations could arise from unaccounted perturbers in the MQDT or from channel interactions with additional $(F = 3/2)^e$ Rydberg series. In the case of $F = 5/2$, we additionally observe slight deviations between experiment and theory that could be caused by uncompensated stray electric fields.

There is only a single $D$ Rydberg series with $F = 1/2$ ($F = 7/2$) converging to the $F_c = 1$ threshold with $^3D_1$ ($^3D_3$) character. Because we use the $6s6p\ ^1P_1(F = 3/2)$ (dominantly singlet character) state as an intermediate state, the $|\nu, L = 2, F = 1/2\rangle$ (dominantly triplet character) and the $|\nu, L = 2, F = 7/2\rangle$ Rydberg states are inaccessible by direct laser spectroscopy. However, the fitted $F = 3/2$ and $F = 5/2$ series MQDT models include a Rydberg-Ritz model for the $^3D_1$ and $^3D_3$ series (Supplemental Material Tables S9 and S10 [70]). Therefore, we use this model to predict the positions of the $F = 1/2$ and $F = 7/2$ series.

## APPENDIX F: POLARIZABILITY TRENDS IN $^{174}$Yb AND $^{171}$Yb $S$ RYDBERG STATES

In Figs. 20 and 21, we present predicted polarizabilities for $L = 0$ states of both $^{174}$Yb and $^{171}$Yb. We note several interesting features. First, the $^{174}$Yb $^3S_1$ polarizability is

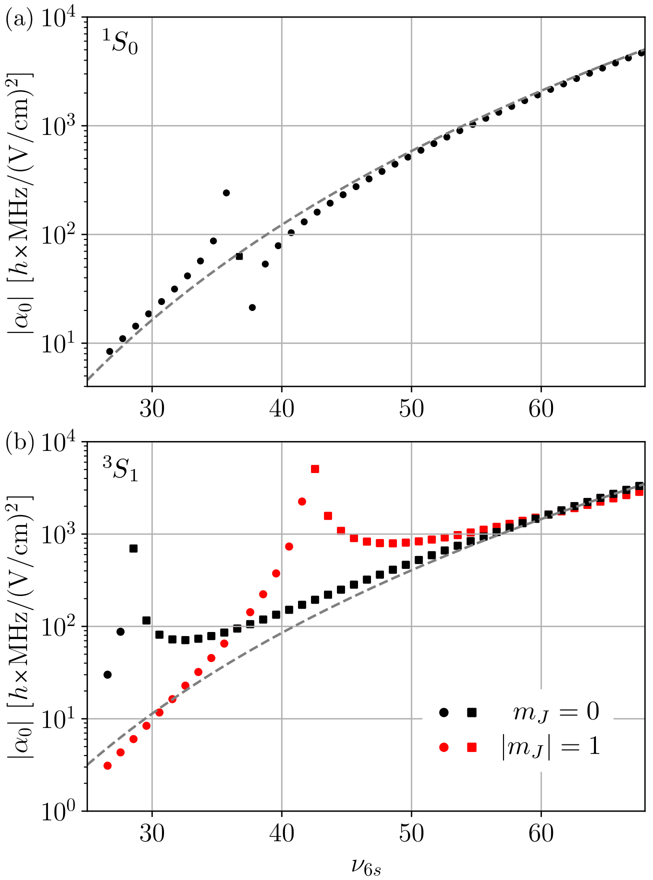

FIG. 20. Predicted absolute static dipole polarizabilities of Rydberg series of $^{174}$Yb for (a) $6sns\ ^1S_0$ and (b) $6sns\ ^3S_1$. Circles indicate positive values of $\alpha_0$, whereas squares indicate negative values of $\alpha_0$. The gray dashed lines in (a) and (b) serve as a guide to the eye, indicating a $\nu_{6s}^7$ scaling.

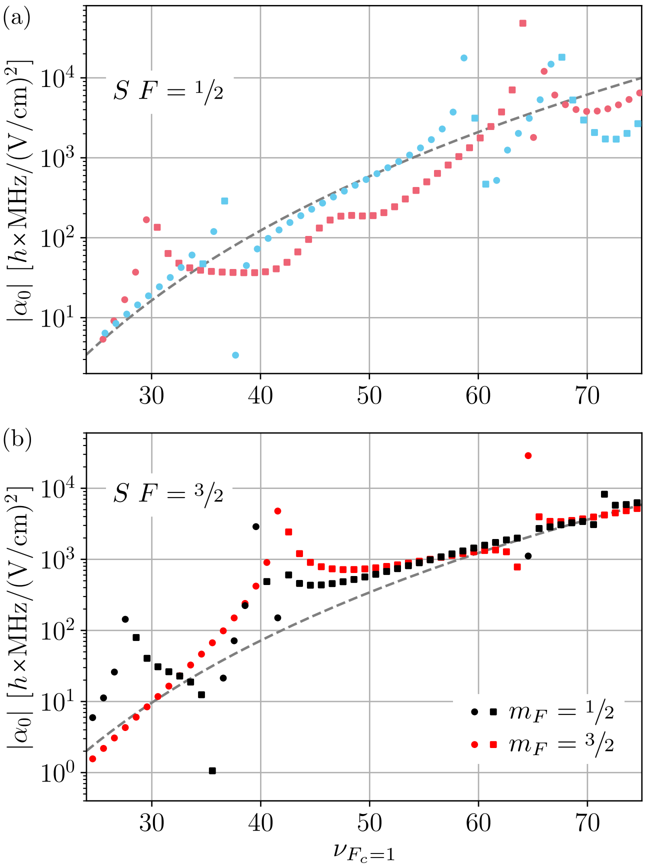

FIG. 21. Predicted absolute static dipole polarizabilities of Rydberg series of $^{171}$Yb with (a) $S\ F = 1/2$ (color code as in Fig. 3) and (b) $S\ F = 3/2$. Circles indicate positive values of $\alpha_0$, whereas squares indicate negative values of $\alpha_0$. The gray dashed lines in (a) and (b) serve as a guide to the eye, indicating a $\nu_{F_c=1}^7$ scaling.

positive at low $n$ and negative at high $n$, as the strongly perturbed $^3P_0$ and $^3P_1$ series cross the $^3S_1$ series in energy. Second, the $^{171}$Yb polarizabilities have a much more complex behavior, with multiple sign changes resulting from a number of resonances.

## APPENDIX G: RYDBERG-RYDBERG-INTERACTION TRENDS

The van der Waals coefficients $C_6$ for the $L = 0$ Rydberg states of $^{174}$Yb and $^{171}$Yb Rydberg states are presented in Fig. 22. In $^{174}$Yb, the $C_6$ coefficients of $6sns\ ^1S_0$ Rydberg series are unusually small, consistent with the single-channel calculations of Ref. [89] (we additionally note a Förster resonance around $\nu \approx 50$, which arises from the inclusion of singlet-triplet mixing in the $^{1,3}P_1$ Rydberg series). Similar Förster resonances have also been predicted for $^3D_2$ and $^{1,3}F_3$ states of $^{88}$Sr [68]. In contrast, the $C_6$ coefficients of $6sns\,^3S_1$ Rydberg states of $^{174}$Yb are larger, consistent with previous estimates [29] and observations [99], but calculated here for the first time. The $C_6$ coefficients of this series are the same magnitude as for the $ns_{1/2}$ Rydberg states of rubidium, but with opposite sign (i.e., attractive).

As in the case for $^1S_0$ Rydberg states of $^{174}$Yb, the singlet-connected $|\nu, L = 0, F = 1/2\rangle$ Rydberg states of $^{171}$Yb (blue dots in Fig. 22) have small $C_6$ coefficients in the range $40 \leq \nu \leq 70$. The triplet connected $|\nu, L = 0, F = 1/2, m_F\rangle$ states have $C_6$ coefficients that are approximately half the magnitude of Rb, with the same sign (i.e., repulsive).

As pointed out in Sec. IV, $|\nu, L = 0, F = 3/2\rangle|\nu, L = 0, F = 3/2\rangle$ Rydberg-pair states of $^{171}$Yb have small Förster defects over a large range of effective principal quantum

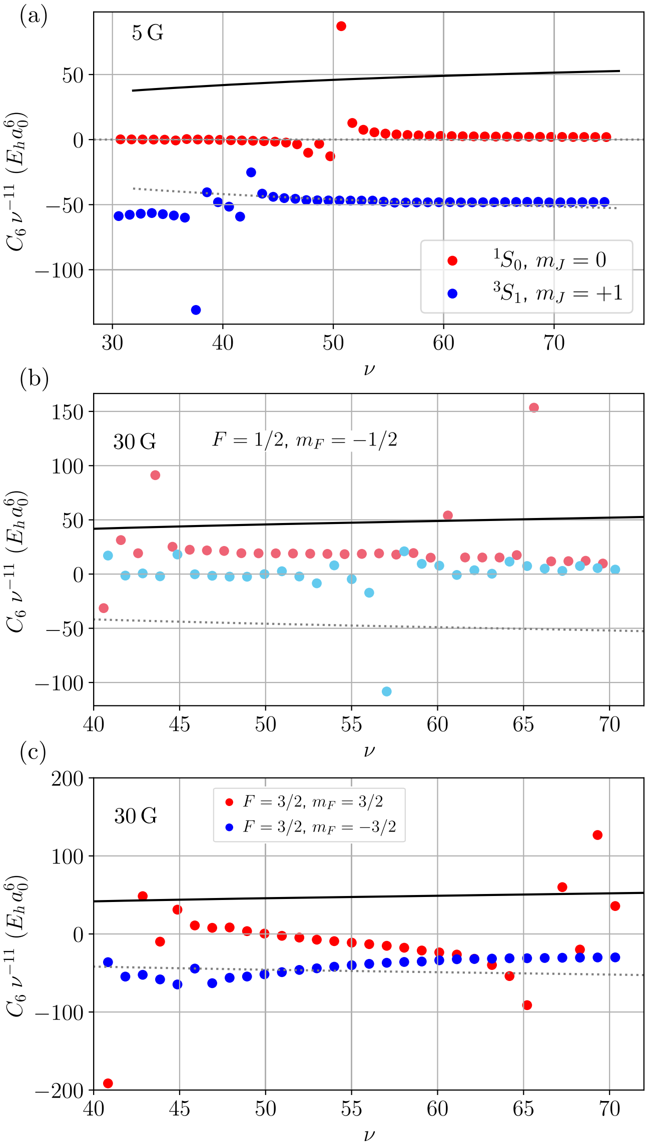

FIG. 22. Predicted scaled $C_6$ coefficients of (a) $^{174}$Yb $^1S_0$ (red dots) and $^3S_1$ (blue dots) Rydberg states at a magnetic field of 5 G ($\theta = \pi/2$). (b),(c) $^{171}$Yb $|\nu, L = 0, F = 1/2\rangle$ and $|\nu, L = 0, F = 3/2\rangle$ Rydberg states at a magnetic field of 30 G ($\theta = \pi/2$). $\theta$ is the angle between the magnetic field and the interatomic axis. For comparison, the scaled $C_6$ coefficients of $n\,^2S_{1/2}$ Rydberg states of Rb are given by solid ($C_6$) and dotted ($-C_6$) black lines. The color code in (b) corresponds to the color code in Fig. 3.

number $\nu$ (Fig. 23). It is surprising that the Förster defect is so small over such a large range of $\nu$, which results from a combination of series perturbers and hyperfine coupling. To calculate a meaningful asymptotic $C_6$ coefficient, we calculate the pair potentials under a 30-G magnetic field to lift the degeneracy somewhat [Fig. 22(c)]. The extracted $C_6$ coefficients are not meaningful at short separations, which are dominated by resonant dipole-dipole interaction, as shown in Fig. 7.

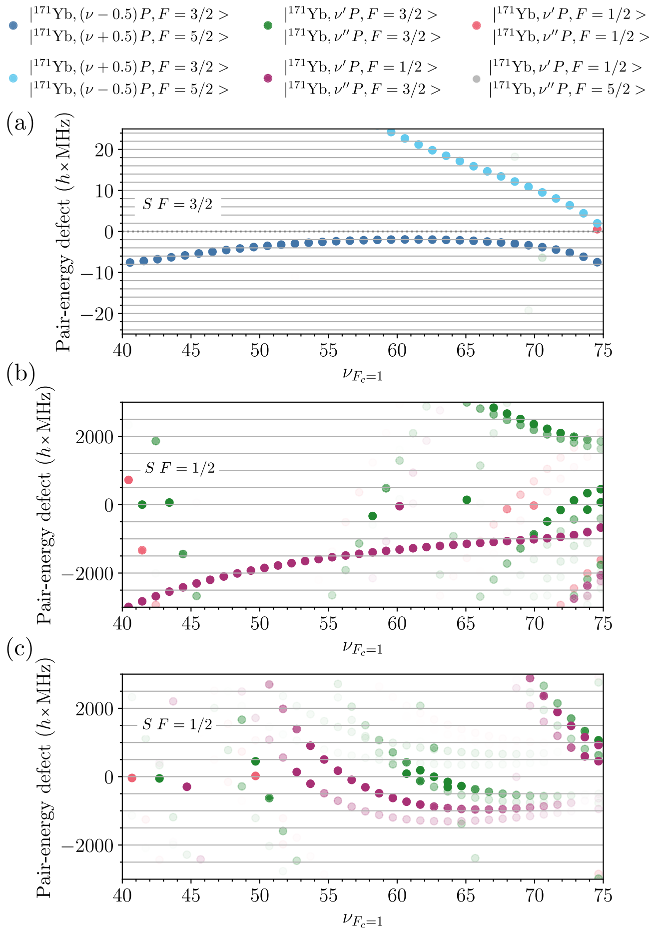

FIG. 23. $^{171}$Yb pair-energy defects between $|\nu_{F_c=1}, L = 0, F\rangle|\nu_{F_c=1}, L = 0, F\rangle$ and the nearest dipole-coupled $|\nu_{F_c=1}, L = 1, F\rangle|\nu_{F_c=1}, L = 1, F'\rangle$ states for (a) $F = 3/2$, and (b) and (c) $F = 1/2$. The color of the markers indicates the combination of hyperfine states of the $|\nu, L = 1, F\rangle|\nu', L = 1, F'\rangle$ pair state according to the legend. The opacity encodes $[(d_1 d_2)^2/\Delta E]$ $(1/\nu_{F_c=1})^8$, where $d_i$ are the dipole matrix elements between the involved Rydberg states, and $\Delta E$ corresponds to the pair defect.

* * *

[1] H. Bernien, S. Schwartz, A. Keesling, H. Levine, A. Omran, H. Pichler, S. Choi, A. S. Zibrov, M. Endres, M. Greiner, V. Vuletić, and M. D. Lukin, *Probing many-body dynamics on a 51-atom quantum simulator*, Nature (London) **551**, 579 (2017).

[2] P. Scholl, M. Schuler, H. J. Williams, A. A. Eberharter, D. Barredo, K.-N. Schymik, V. Lienhard, L.-P. Henry, T. C. Lang, T. Lahaye, A. M. Läuchli, and A. Browaeys, *Quantum simulation of 2D antiferromagnets with hundreds of Rydberg atoms*, Nature (London) **595**, 233 (2021).

[3] D. Bluvstein, H. Levine, G. Semeghini, T. T. Wang, S. Ebadi, M. Kalinowski, A. Keesling, N. Maskara, H. Pichler, M. Greiner, V. Vuletić, and M. D. Lukin,

*A quantum processor based on coherent transport of entangled atom arrays*, Nature (London) **604**, 451 (2022).

[4] W. J. Eckner, N. Darkwah Oppong, A. Cao, A. W. Young, W. R. Milner, J. M. Robinson, J. Ye, and A. M. Kaufman, *Realizing spin squeezing with Rydberg interactions in an optical clock*, Nature (London) **621**, 734 (2023).

[5] P. Goy, J. M. Raimond, G. Vitrant, and S. Haroche, *Millimeter-wave spectroscopy in cesium Rydberg states. Quantum defects, fine- and hyperfine-structure measurements*, Phys. Rev. A **26**, 2733 (1982).

[6] K.-H. Weber and C. J. Sansonetti, *Accurate energies of nS, nP, nD, nF, and nG levels of neutral cesium*, Phys. Rev. A **35**, 4650 (1987).

[7] W. Li, I. Mourachko, M. W. Noel, and T. F. Gallagher, *Millimeter-wave spectroscopy of cold Rb Rydberg atoms in a magneto-optical trap: Quantum defects of the ns, np, and nd series*, Phys. Rev. A **67**, 052502 (2003).

[8] M. Mack, F. Karlewski, H. Hattermann, S. Höckh, F. Jessen, D. Cano, and J. Fortágh, *Measurement of absolute transition frequencies of* $^{87}$Rb *to nS and nD Rydberg states by means of electromagnetically induced transparency*, Phys. Rev. A **83**, 052515 (2011).

[9] J. Han, Y. Jamil, D. V. L. Norum, P. J. Tanner, and T. F. Gallagher, Rb *nf quantum defects from millimeter-wave spectroscopy of cold* $^{85}$Rb *Rydberg atoms*, Phys. Rev. A **74**, 054502 (2006).

[10] J. Deiglmayr, H. Herburger, H. Saßmannshausen, P. Jansen, H. Schmutz, and F. Merkt, *Precision measurement of the ionization energy of* Cs *i*, Phys. Rev. A **93**, 013424 (2016).

[11] M. Peper, F. Helmrich, J. Butscher, J. A. Agner, H. Schmutz, F. Merkt, and J. Deiglmayr, *Precision measurement of the ionization energy and quantum defects of* $^{39}$K *i*, Phys. Rev. A **100**, 012501 (2019).

[12] M. L. Zimmerman, M. G. Littman, M. M. Kash, and D. Kleppner, *Stark structure of the Rydberg states of alkali-metal atoms*, Phys. Rev. A **20**, 2251 (1979).

[13] C. E. Theodosiou, *Lifetimes of alkali-metal—atom Rydberg states*, Phys. Rev. A **30**, 2881 (1984).

[14] J. Deiglmayr, *Long-range interactions between Rydberg atoms*, Phys. Scr. **91**, 104007 (2016).

[15] L. Béguin, A. Vernier, R. Chicireanu, T. Lahaye, and A. Browaeys, *Direct measurement of the van der Waals interaction between two Rydberg atoms*, Phys. Rev. Lett. **110**, 263201 (2013).

[16] S. Ravets, H. Labuhn, D. Barredo, T. Lahaye, and A. Browaeys, *Measurement of the angular dependence of the dipole-dipole interaction between two individual Rydberg atoms at a Förster resonance*, Phys. Rev. A **92**, 020701(R) (2015).

[17] S. Anand, C. E. Bradley, R. White, V. Ramesh, K. Singh, and H. Bernien, *A dual-species Rydberg array*, Nat. Phys. **20**, 1744 (2024).

[18] W. P. Spencer, A. G. Vaidyanathan, D. Kleppner, and T. W. Ducas, *Measurements of lifetimes of sodium Rydberg states in a cooled environment*, Phys. Rev. A **24**, 2513 (1981).

[19] W. P. Spencer, A. G. Vaidyanathan, D. Kleppner, and T. W. Ducas, *Temperature dependence of blackbody-radiation-induced transfer among highly excited states of sodium*, Phys. Rev. A **25**, 380 (1982).

[20] H. Bergström, C. Levinson, and H. Lundberg, *Natural radiative lifetimes in the* $5snd\ ^1D_2$ *series of* Sr *I*, Z. Phys. D **2**, 127 (1986).

[21] C. Boisseau, I. Simbotin, and R. Côté, *Macrodimers: Ultralong range Rydberg molecules*, Phys. Rev. Lett. **88**, 133004 (2002).

[22] K. R. Overstreet, A. Schwettmann, J. Tallant, D. Booth, and J. P. Shaffer, *Observation of electric-field-induced* Cs *Rydberg atom macrodimers*, Nat. Phys. **5**, 581 (2009).

[23] H. Saßmannshausen and J. Deiglmayr, *Observation of Rydberg-atom macrodimers: Micrometer-sized diatomic molecules*, Phys. Rev. Lett. **117**, 083401 (2016).

[24] S. Hollerith, J. Zeiher, J. Rui, A. Rubio-Abadal, V. Walther, T. Pohl, D. M. Stamper-Kurn, I. Bloch, and C. Gross, *Quantum gas microscopy of Rydberg macrodimers*, Science **364**, 664 (2019).

[25] A. Cooper, J. P. Covey, I. S. Madjarov, S. G. Porsev, M. S. Safronova, and M. Endres, *Alkaline-earth atoms in optical tweezers*, Phys. Rev. X **8**, 041055 (2018).

[26] M. A. Norcia, A. W. Young, and A. M. Kaufman, *Microscopic control and detection of ultracold strontium in optical-tweezer arrays*, Phys. Rev. X **8**, 041054 (2018).

[27] R. C. Teixeira, A. Larrouy, A. Muni, L. Lachaud, J.-M. Raimond, S. Gleyzes, and M. Brune, *Preparation of long-lived, non-autoionizing circular Rydberg states of strontium*, Phys. Rev. Lett. **125**, 263001 (2020).

[28] C. Hölzl, A. Götzelmann, E. Pultinevicius, M. Wirth, and F. Meinert, *Long-lived circular Rydberg qubits of alkaline-earth atoms in optical tweezers*, Phys. Rev. X **14**, 021024 (2024).

[29] J. T. Wilson, S. Saskin, Y. Meng, S. Ma, R. Dilip, A. P. Burgers, and J. D. Thompson, *Trapping alkaline earth Rydberg atoms optical tweezer arrays*, Phys. Rev. Lett. **128**, 033201 (2022).

[30] A. Jenkins, J. W. Lis, A. Senoo, W. F. McGrew, and A. M. Kaufman, *Ytterbium nuclear-spin qubits in an optical tweezer array*, Phys. Rev. X **12**, 021027 (2022).

[31] S. Ma, A. P. Burgers, G. Liu, J. Wilson, B. Zhang, and J. D. Thompson, *Universal gate operations on nuclear spin qubits in an optical tweezer array of* $^{171}$Yb *atoms*, Phys. Rev. X **12**, 021028 (2022).

[32] W. Huie, L. Li, N. Chen, X. Hu, Z. Jia, Won Kyu Calvin Sun, and J. P. Covey, *Repetitive readout and real-time control of nuclear spin qubits in* $^{171}$Yb *atoms*, PRX Quantum **4**, 030337 (2023).

[33] P. Scholl, A. L. Shaw, R. B.-S. Tsai, R. Finkelstein, J. Choi, and M. Endres, *Erasure conversion in a high-fidelity Rydberg quantum simulator*, Nature (London) **622**, 273 (2023).

[34] A. L. Shaw, Z. Chen, J. Choi, D. K. Mark, P. Scholl, R. Finkelstein, A. Elben, S. Choi, and M. Endres, *Benchmarking highly entangled states on a 60-atom analogue quantum simulator*, Nature (London) **628**, 71 (2024).

[35] R. Finkelstein, R. B.-S. Tsai, X. Sun, P. Scholl, S. Direkci, T. Gefen, J. Choi, A. L. Shaw, and M. Endres, *Universal quantum operations and ancilla-based read-out for tweezer clocks*, Nature (London) **634**, 321 (2024).

[36] A. Cao, W. J. Eckner, T. Lukin Yelin, A. W. Young, S. Jandura, L. Yan, K. Kim, G. Pupillo, J. Ye, N. Darkwah Oppong, and A. M. Kaufman, *Multi-qubit gates*

*and Schrödinger cat states in an optical clock*, Nature (London) **634**, 315 (2024).

[37] J. W. Lis, A. Senoo, W. F. McGrew, F. Rönchen, A. Jenkins, and A. M. Kaufman, *Midcircuit Operations using the omg architecture in neutral atom arrays*, Phys. Rev. X **13**, 041035 (2023).

[38] M. A. Norcia *et al.*, *Midcircuit qubit measurement and rearrangement in a* $^{171}$Yb *atomic array*, Phys. Rev. X **13**, 041034 (2023).

[39] Y. Wu, S. Kolkowitz, S. Puri, and J. D. Thompson, *Erasure conversion for fault-tolerant quantum computing in alkaline earth Rydberg atom arrays*, Nat. Commun. **13**, 4657 (2022).

[40] S. Ma, G. Liu, P. Peng, B. Zhang, S. Jandura, J. Claes, A. P. Burgers, G. Pupillo, S. Puri, and J. D. Thompson, *High-fidelity gates and mid-circuit erasure conversion in an atomic qubit*, Nature (London) **622**, 279 (2023).

[41] M. J. Seaton, *Quantum defect theory I. General formulation*, Proc. Phys. Soc. London **88**, 801 (1966).

[42] U. Fano, *Quantum Defect theory of l uncoupling in* $H_2$ *as an example of channel-interaction treatment*, Phys. Rev. A **2**, 353 (1970).

[43] C. L. Vaillant, M. P. A. Jones, and R. M. Potvliege, *Multichannel quantum defect theory of strontium bound Rydberg states*, J. Phys. B **47**, 155001 (2014).

[44] F. Robicheaux, D. W. Booth, and M. Saffman, *Theory of long-range interactions for Rydberg states attached to hyperfine-split cores*, Phys. Rev. A **97**, 022508 (2018).

[45] E. Robertson, N. Šibalić, R. Potvliege, and M. Jones, *ARC3.0: An expanded PYTHON toolbox for atomic physics calculations*, Comput. Phys. Commun. **261**, 107814 (2021).

[46] M. Aymar, A. Débarre, and O. Robaux, *Highly excited levels of neutral ytterbium. II. Multichannel quantum defect analysis of odd- and even-parity spectra*, J. Phys. B **13**, 1089 (1980).

[47] M. Aymar, *Multichannel-quantum-defect theory wave functions of* Ba *tested or improved by laser measurements*, J. Opt. Soc. Am. B **1**, 239 (1984).

[48] R. Ali, M. Yaseen, A. Nadeem, S. A. Bhatti, and M. A. Baig, *Two-colour three-photon excitation of the* $6snf$ $^{1,3}F_3$ *and* $6snp$ $^1P_1$, $^3P_{1,2}$ *Rydberg levels of* Yb i, J. Phys. B **32**, 953 (1999).

[49] H. Lehec, A. Zuliani, W. Maineult, E. Luc-Koenig, P. Pillet, P. Cheinet, F. Niyaz, and T. F. Gallagher, *Laser and microwave spectroscopy of even-parity Rydberg states of neutral ytterbium and multichannel-quantum-defect-theory analysis*, Phys. Rev. A **98**, 062506 (2018).

[50] H. Lehec, *Spectroscopie Rydberg et excitation du coeur isolé d'atomes d'ytterbium ultra-froids*, Ph.D. thesis, Université Paris Saclay, 2017.

[51] R. Ding, J. D. Whalen, S. K. Kanungo, T. C. Killian, F. B. Dunning, S. Yoshida, and J. Burgdörfer, *Spectroscopy of* $^{87}$Sr *triplet Rydberg states*, Phys. Rev. A **98**, 042505 (2018).

[52] F. Robicheaux, *Calculations of long range interactions for* $^{87}$Sr *Rydberg states*, J. Phys. B **52**, 244001 (2019).

[53] P. Camus and F. S. Tomkins, *Spectre d'absorption de* Yb *I*, J. Phys. (Paris) **30**, 545 (1969).

[54] W. F. Meggers and J. L. Tech, *The first spectrum of ytterbium (*Yb *I)*, J. Res. Natl. Bur. Stand. **83**, 13 (1977).

[55] P. Camus, A. Débarre, and C. Morillon, *Highly excited levels of neutral ytterbium. I. Two-photon and two-step spectroscopy of even spectra*, J. Phys. B **13**, 1073 (1980).

[56] M. Aymar, R. J. Champeau, C. Delsart, and O. Robaux, *Three-step laser spectroscopy and multichannel quantum defect analysis of odd-parity Rydberg states of neutral ytterbium*, J. Phys. B **17**, 3645 (1984).

[57] J. Neukammer, H. Rinneberg, and U. Majewski, *Diamagnetic shift and singlet-triplet mixing of* $6snp$ Yb *Rydberg states with large radial extent*, Phys. Rev. A **30**, 1142 (1984).

[58] H. Maeda, Y. Matsuo, M. Takami, and A. Suzuki, *Optical-microwave double-resonance spectroscopy of highly excited Rydberg states of ytterbium*, Phys. Rev. A **45**, 1732 (1992).

[59] R. Zerne, L. Caiyan, J. Zhankui, and J. Larsson, *Landé* $g_J$ *factor measurements in the* $6snd$ $^{1,3}D_2$ *sequences of* Yb *I*, Z. Phys. D **37**, 259 (1996).

[60] F. Niyaz, J. Nunkaew, and T. F. Gallagher, *Microwave spectroscopy of the* Yb $6s(n+3)d \to 6sng$, $6snh$, *and* $6sni$ *transitions*, Phys. Rev. A **99**, 042507 (2019).

[61] D. Okuno, Y. Nakamura, T. Kusano, Y. Takasu, N. Takei, H. Konishi, and Y. Takahashi, *High-resolution spectroscopy and single-photon Rydberg excitation of reconfigurable ytterbium atom tweezer arrays utilizing a metastable state*, J. Phys. Soc. Jpn. **91**, 084301 (2022).

[62] K. T. Lu, *Spectroscopy and collision theory. The* Xe *absorption spectrum*, Phys. Rev. A **4**, 579 (1971).

[63] K. Barnes *et al.*, *Assembly and coherent control of a register of nuclear spin qubits*, Nat. Commun. **13**, 2779 (2022).

[64] J. Hostetter, J. D. Pritchard, J. E. Lawler, and M. Saffman, *Measurement of holmium Rydberg series through magneto-optical trap depletion spectroscopy*, Phys. Rev. A **91**, 012507 (2015).

[65] A. Trautmann, M. J. Mark, P. Ilzhöfer, H. Edri, A. E. Arrach, J. G. Maloberti, C. H. Greene, F. Robicheaux, and F. Ferlaino, *Spectroscopy of Rydberg states in erbium using electromagnetically induced transparency*, Phys. Rev. Res. **3**, 033165 (2021).

[66] M. J. Seaton, *Quantum defect theory*, Rep. Prog. Phys. **46**, 167 (1983).

[67] W. E. Cooke and C. L. Cromer, *Multichannel quantum-defect theory and an equivalent N-level system*, Phys. Rev. A **32**, 2725 (1985).

[68] C. L. Vaillant, R. M. Potvliege, and M. P. A. Jones, *Intercombination effects in resonant energy transfer*, Phys. Rev. A **92**, 042705 (2015).

[69] T. F. Gallagher, *Rydberg Atoms*, Cambridge Monographs on Atomic, Molecular and Chemical Physics (Cambridge University Press, Cambridge, England, 1994).

[70] See Supplemental Material at http://link.aps.org/supplemental/10.1103/PhysRevX.15.011009 for tables of the developed MQDT models and tables of previous [12,46,48–50,53–56,58,59,71–74] and new spectroscopic data used in the fitting and testing of the MQDT models.

[71] U. Majewski, *Hochauflösende Laserspektroskopie von Ytterbium-Rydbergzuständen*, Diploma thesis, Freie Universität Berlin, 1985.

[72] W. C. Martin, R. Zalubas, and L. Hagan, *Atomic Energy Levels: The Rare Earth Elements*, NBS, National Standards Reference Data Series—60 (U.S. GPO, Washington, DC, 1978).

[73] W. Bi-ru, Z. You-feng, X. Yun-fei, P. Li-gang, L. Ji, and Z. Jian-wei, *The* $6snp\ {}^3\mathrm{P}_{0,2}$ *Rydberg series of neutral ytterbium*, J. Phys. B **24**, 49 (1991).

[74] J.-F. Wyart and P. Camus, *Extended analysis of the emission spectrum of neutral ytterbium (*Yb *I)*, Phys. Scr. **20**, 43 (1979).

[75] R. Beigang, W. Makat, A. Timmermann, and P. J. West, *Hyperfine-induced n mixing in high Rydberg states of* $^{87}$Sr, Phys. Rev. Lett. **51**, 771 (1983).

[76] J.-Q. Sun and K. T. Lu, *Hyperfine structure of extremely high Rydberg msns* $^1\mathrm{S}_0$ *and msns* $^3\mathrm{S}_1$ *series in odd alkaline-earth isotopes*, J. Phys. B **21**, 1957 (1988).

[77] H. J. Wörner, U. Hollenstein, and F. Merkt, *Multichannel quantum defect theory and high-resolution spectroscopy of the hyperfine structure of high Rydberg states of* $^{83}$Kr, Phys. Rev. A **68**, 032510 (2003).

[78] M. Saffman, *Quantum computing with atomic qubits and Rydberg interactions: Progress and challenges*, J. Phys. B **49**, 202001 (2016).

[79] R. Blatt, H. Schnatz, and G. Werth, *Precise determination of the* $^{171}\mathrm{Yb}^+$ *ground state hyperfine separation*, Z. Phys. A **312**, 143 (1983).

[80] P. Liao, R. Freeman, R. Panock, and L. Humphrey, *Hyperfine-induced singlet-triplet mixing in* $^3$He, Opt. Commun. **34**, 195 (1980).

[81] J.-Q. Sun, *Multichannel quantum defect theory of the hyperfine structure of high Rydberg states*, Phys. Rev. A **40**, 7355 (1989).

[82] J.-Q. Sun, K. T. Lu, and R. Beigang, *Hyperfine structure of extremely high Rydberg msn*d $^1\mathrm{D}_2$, $^3\mathrm{D}_1$, $^3\mathrm{D}_2$ *and* $^3\mathrm{D}_3$ *series in odd alkaline-earth isotopes*, J. Phys. B **22**, 2887 (1989).

[83] J. Neukammer and H. Rinneberg, *Hyperfine structure of perturbed* $6sns\ {}^3\mathrm{S}_1$ *Rydberg states of barium*, J. Phys. B **15**, L425 (1982).

[84] L. Barbier and R.-J. Champeau, *Very high resolution study of high Rydberg levels of the configurations* $4f^{14}\,6snd$ *of* Yb *I*, J. Phys. (Paris) **41**, 947 (1980).

[85] U. Majewski, J. Neukammer, and H. Rinneberg, *High-resolution three-photon spectroscopy of* $6s15p\ {}^{1,3}P_1$ *Rydberg states of* Yb, Phys. Rev. Lett. **51**, 1340 (1983).

[86] S. Weber, C. Tresp, H. Menke, A. Urvoy, O. Firstenberg, H. P. Büchler, and S. Hofferberth, *Calculation of Rydberg interaction potentials*, J. Phys. B **50**, 133001 (2017).

[87] N. Šibalić, J. Pritchard, C. Adams, and K. Weatherill, *ARC: An open-source library for calculating properties of alkali Rydberg atoms*, Comput. Phys. Commun. **220**, 319 (2017).

[88] B. Vermersch, *Anisotropy and state mixing in the interactions between Rydberg states*, Eur. Phys. J. Special Topics **225**, 2977 (2016).

[89] C. L. Vaillant, M. P. A. Jones, and R. M. Potvliege, *Long-range Rydberg–Rydberg interactions in calcium, strontium and ytterbium*, J. Phys. B **45**, 135004 (2012).

[90] I. I. Beterov and M. Saffman, *Rydberg blockade, Förster resonances, and quantum state measurements with different atomic species*, Phys. Rev. A **92**, 042710 (2015).

[91] J. T. Young, P. Bienias, R. Belyansky, A. M. Kaufman, and A. V. Gorshkov, *Asymmetric blockade and multiqubit gates via dipole-dipole interactions*, Phys. Rev. Lett. **127**, 120501 (2021).

[92] A. Derevianko, P. Kómár, T. Topcu, R. M. Kroeze, and M. D. Lukin, *Effects of molecular resonances on Rydberg blockade*, Phys. Rev. A **92**, 063419 (2015).

[93] H. Levine, A. Keesling, G. Semeghini, A. Omran, T. T. Wang, S. Ebadi, H. Bernien, M. Greiner, V. Vuletić, H. Pichler, and M. D. Lukin, *Parallel implementation of high-fidelity multiqubit gates with neutral atoms*, Phys. Rev. Lett. **123**, 170503 (2019).

[94] S. Jandura and G. Pupillo, *Time-optimal two- and three-qubit gates for Rydberg atoms*, Quantum **6**, 712 (2022).

[95] S. J. Evered, D. Bluvstein, M. Kalinowski, S. Ebadi, T. Manovitz, H. Zhou, S. H. Li, A. A. Geim, T. T. Wang, N. Maskara, H. Levine, G. Semeghini, G. Greiner, G. Vuletić, and M. D. Lukin, *High-fidelity parallel entangling gates on a neutral atom quantum computer*, Nature (London) **622**, 268 (2023).

[96] E. Knill, D. Leibfried, R. Reichle, J. Britton, R. B. Blakestad, J. D. Jost, C. Langer, R. Ozeri, S. Seidelin, and D. J. Wineland, *Randomized benchmarking of quantum gates*, Phys. Rev. A **77**, 012307 (2008).

[97] G. Lochead, D. Boddy, D. P. Sadler, C. S. Adams, and M. P. A. Jones, *Number-resolved imaging of excited-state atoms using a scanning autoionization microscope*, Phys. Rev. A **87**, 053409 (2013).

[98] I. S. Madjarov, J. P. Covey, A. L. Shaw, J. Choi, A. Kale, A. Cooper, H. Pichler, V. Schkolnik, J. R. Williams, and M. Endres, *High-fidelity entanglement and detection of alkaline-earth Rydberg atoms*, Nat. Phys. **16**, 857 (2020).

[99] A. P. Burgers, S. Ma, S. Saskin, J. Wilson, M. A. Alarcón, C. H. Greene, and J. D. Thompson, *Controlling Rydberg excitations using ion-core transitions in alkaline-earth atom-tweezer arrays*, PRX Quantum **3**, 020326 (2022).

[100] K.-L. Pham, T. F. Gallagher, P. Pillet, S. Lepoutre, and P. Cheinet, *Coherent light shift on alkaline-earth Rydberg atoms from isolated core excitation without autoionization*, PRX Quantum **3**, 020327 (2022).

[101] A. D. Ludlow, M. M. Boyd, J. Ye, E. Peik, and P. O. Schmidt, *Optical atomic clocks*, Rev. Mod. Phys. **87**, 637 (2015).

[102] V. D. Ovsiannikov, A. Derevianko, and K. Gibble, *Rydberg spectroscopy in an optical lattice: Blackbody thermometry for atomic clocks*, Phys. Rev. Lett. **107**, 093003 (2011).

[103] C.-M. Lee and K. T. Lu, *Spectroscopy and collision theory. II. The* Ar *absorption spectrum*, Phys. Rev. A **8**, 1241 (1973).

[104] M. Aymar, O. Robaux, and C. Thomas, *Theoretical investigations on the bound odd-parity spectrum of neutral krypton*, J. Phys. B **14**, 4255 (1981).

[105] M. Schäfer, M. Raunhardt, and F. Merkt, *Millimeter-wave spectroscopy and multichannel quantum-defect-theory analysis of high Rydberg states of xenon: The hyperfine structure of* $^{129}\mathrm{Xe}^+$ *and* $^{131}\mathrm{Xe}^+$, Phys. Rev. A **81**, 032514 (2010).

[106] R. Beigang, K. Lücke, D. Schmidt, A. Timmermann, and P. West, *One-photon laser spectroscopy of Rydberg series from metastable levels in calcium and strontium*, Phys. Scr. **26**, 183 (1982).

[107] H. Rinneberg and J. Neukammer, *Hyperfine structure and three-channel quantum-defect theory of* $6snd^1D_2$ *Rydberg states of* Ba, Phys. Rev. A **27**, 1779 (1983).

[108] M. Aymar, *Rydberg series of alkaline-earth atoms* Ca *through* Ba*. The interplay of laser spectroscopy and multichannel quantum defect analysis*, Phys. Rep. **110**, 163 (1984).

[109] S. Bhattacharyya, M. A. N. Razvi, S. Cohen, and S. G. Nakhate, *Odd-parity* $J = 11/2$ *autoionizing Rydberg series of europium below the* $5d\,^9D_4$ *threshold: Spectroscopy and multichannel quantum-defect-theory analysis*, Phys. Rev. A **76**, 012502 (2007).

[110] A. Osterwalder, A. Wüest, F. Merkt, and C. Jungen, *High-resolution millimeter wave spectroscopy and multichannel quantum defect theory of the hyperfine structure in high Rydberg states of molecular hydrogen* $H_2$, J. Chem. Phys. **121**, 11810 (2004).

[111] D. Sprecher, C. Jungen, and F. Merkt, *Determination of the binding energies of the* $np$ *Rydberg states of* $H_2$, HD*, and* $D_2$ *from high-resolution spectroscopic data by multichannel quantum-defect theory*, J. Chem. Phys. **140**, 104303 (2014).

[112] RYDCALC, https://github.com/ThompsonLabPrinceton/rydcalc.

[113] C. H. Greene and M. Aymar, *Spin-orbit effects in the heavy alkaline-earth atoms*, Phys. Rev. A **44**, 1773 (1991).

[114] A. R. Edmonds, *Angular Momentum in Quantum Mechanics*, 4th ed. (Princeton University Press, Princeton, NJ, 1996).

[115] O. Robaux and M. Aymar, *A program for analysing the Rydberg series of highly excited discrete spectra by M.Q.D.T.*, Comput. Phys. Commun. **25**, 223 (1982).

[116] R. R. Freeman and D. Kleppner, *Core polarization and quantum defects in high-angular-momentum states of alkali atoms*, Phys. Rev. A **14**, 1614 (1976).

[117] S. A. Bhatti, C. L. Cromer, and W. E. Cooke, *Analysis of the Rydberg character of the* $5d7d\,^1D_2$ *state of barium*, Phys. Rev. A **24**, 161 (1981).

[118] F. A. Jenkins and E. Segrè, *The quadratic Zeeman effect*, Phys. Rev. **55**, 52 (1939).

[119] K. Singer, M. Reetz-Lamour, T. Amthor, S. Fölling, M. Tscherneck, and M. Weidemüller, *Spectroscopy of an ultracold Rydberg gas and signatures of Rydberg–Rydberg interactions*, J. Phys. B **38**, S321 (2005).

[120] M. E. Rose, *The electrostatic interaction of two arbitrary charge distributions*, J. Math. Phys. **37**, 215 (1958).

[121] A. Dalgarno and W. Davison, *The calculation of van der Waals interactions* (Academic Press, New York, 1966), pp. 1–32.

[122] M. Kleinert, M. E. Gold Dahl, and S. Bergeson, *Measurement of the* Yb $I$ $^1S_0 - {}^1P_1$ *transition frequency at 399 nm using an optical frequency comb*, Phys. Rev. A **94**, 052511 (2016).

[123] I. I. Beterov, I. I. Ryabtsev, D. B. Tretyakov, and V. M. Entin, *Quasiclassical calculations of blackbody-radiation-induced depopulation rates and effective lifetimes of Rydberg* $ns$*,* $np$*, and* $nd$ *alkali-metal atoms with* $n \leq 80$, Phys. Rev. A **79**, 052504 (2009).

[124] J. T. Wilson, *New tools for quantum science in* Yb *Rydberg atom arrays*, Ph.D. thesis, Princeton University, 2022.